KU LEUVEN

Citation	Laurens Coox, Francesco Greco, Onur Atak, Dirk Vandepitte, Wim Desmet, (2017), **A robust patch coupling method for NURBS-based isogeometric analysis of non-conforming multipatch surfaces** Comput. Methods Appl. Mech. Engrg., 316, 235-260.
Archived version	Author manuscript: the content is identical to the content of the published paper, but without the final typesetting by the publisher
Published version	http://dx.doi.org/10.1016/j.cma.2016.06.022
Journal homepage	http://www.journals.elsevier.com/computer-methods-in-applied-mechanics-and-engineering/
Author contact	Laurens.Coox@mech.kuleuven.be *+ 32 (0)16 32 28 47*
IR	https://lirias.kuleuven.be/handle/123456789/542529

(article begins on next page)



A robust patch coupling method for NURBS-based isogeometric analysis of non-conforming multipatch surfaces

Laurens Coox[a,b,*], Francesco Greco[a,b], Onur Atak[c], Dirk Vandepitte[a,b], Wim Desmet[a,b]

[a] *KU Leuven, Department of Mechanical Engineering, Celestijnenlaan 300 box 2420, B-3001 Leuven, Belgium*
[b] *Member of Flanders Make*
[c] *Siemens Industry Software NV, Digital Factory, Product Lifecycle Management – Simulation and Test Solutions, Interleuvenlaan 68, B-3001 Leuven, Belgium*

Abstract

This paper presents a simple yet flexible method for coupling non-conforming NURBS patches in isogeometric frameworks. It consists of virtually refining bordering patches to derive coupling constraints in a master-slave formulation. These constraints are then enforced via a substitution method for condensation of the slave variables, thereby reducing the model size. In the special case of hierarchical meshes, the method results in an exact connection. For an arbitrary non-conforming configuration, the master-slave formulation takes the interface constraints into account in a least-squares sense. This yields an accurate weak coupling without overconstraining the interface. The coupling relationships only depend on the mesh itself and not on any problem-dependent parameters, allowing them to be generated in a pre-processing step with very limited numerical efforts. Besides this low computational cost, the main merit of the proposed method lies in its simplicity and robustness, yielding good results for arbitrarily strongly non-conforming patch configurations. Several numerical examples are studied for different problem types requiring C^0- or C^1-continuity, in particular time-harmonic acoustics and (dynamic) thin plate bending. Benchmarking of the proposed approach against existing similar techniques illustrates its superior accuracy and robustness.

Keywords: isogeometric analysis, multipatch coupling, non-conforming patches, NURBS

1. Introduction

IsoGeometric Analysis (IGA) is a numerical technique introduced by Hughes et al. [1, 2]. It addresses the problem that geometry representations in Computer Aided Design (CAD) on the one hand and in Computer Aided Analysis (CAE) on the other hand are very different and mostly incompatible with each other. IGA aims at bridging this gap between design and analysis by introducing CAD descriptions into a CAE environment, and can be seen as a generalisation of the Finite Element Method (FEM). The conventional element-based discretisation and the associated (usually low-order polynomial) shape function expansions are replaced by CAD-based mappings and associated functions, typically Non-Uniform Rational B-Splines (NURBS) or other spline-based descriptions.

*Corresponding author. Tel.: +32 16 32 28 47.
Email address: Laurens.Coox@mech.kuleuven.be (Laurens Coox)

Post-print accepted by Comput. Methods Appl. Mech. Engrg. *June 18, 2016*
Publisher's version available at http://dx.doi.org/10.1016/j.cma.2016.06.022.

IGA has already been studied extensively and applied successfully in various fields of research, as illustrated by the overview presented in [3].

Nonetheless, there are still several open issues when applying IGA in a NURBS-based context, such as the lack of inherent local refinement procedures or the difficulties with straightforwardly creating volumetric geometries. These limitations follow from the fact that CAD geometries are typically built up from NURBS surfaces, which have a tensor-product structure. Moreover, this tensor-product topology makes it difficult to create free-form geometries using a single NURBS surface patch, meaning that complex geometries usually consist of several patches. Unfortunately, these patches in general have non-conforming discretisations and are not mathematically connected to each other on a parametric level. This is not a real issue in design environments, but it requires the patches to be explicitly coupled for analysis purposes, which in a general case cannot be done straightforwardly or even exactly. Other spline-based descriptions such as T-splines [4, 5], subdivision surfaces [6, 7] or PHT-splines [8], allow local refinement and make it easier to create free-form geometries using a single geometric entity. But they have their own drawbacks, the most important one being their incompatibility with most existing CAD environments — which are typically NURBS-based. Staying true to the isogeometric paradigm, it is therefore important for isogeometric frameworks to be able to handle multipatch NURBS geometries.

Several studies have already been conducted regarding the connection of NURBS patches, resulting in a variety of coupling methods. They can be categorised based on two main criteria: the topological nature of the bordering patches, and the required degree of continuity. The topological nature depends purely on the applied discretisation and can refer to properties such as polynomial order, the presence of trimmed parts, or existing gaps or overlaps between patches. But usually the difference in mesh resolution across the interface is the most important topological factor, since a different number of elements on both sides of a patch interface prevents a straightforward coupling. A typical distinction is made between conforming and non-conforming patches, i.e. with matching and non-matching discretisations on their interface. The required degree of continuity is determined by the type of problem under study and refers to the minimally required order of continuity of the function expansion. Usually C^0- or C^1-continuous quantities are required.

Coupling conforming patches with C^0-continuity is trivial because of the one-to-one correspondence of interface variables in that case. Examples can be found in [9], which also treats the less straightforward C^0-coupling of hierarchical patches. The C^1-coupling of conforming patches has been studied extensively because of its importance in isogeometric rotationless shell analysis [10–12]. The bending strip method proposed by Kiendl et al. in [11] adds a strip of fictitious material that introduces a unidirectional bending stiffness to prevent patch interfaces from acting as hinges. Schmidt et al. [13] apply this technique to trimmed (but conforming) NURBS patches for Kirchhoff-Love shell analysis. Rotationless shells consisting of non-conforming NURBS patches are coupled in a C^1-sense in [14], where Lei et al. use a penalty formulation to impose a set of linear constraints derived from the interface knot vectors. The coupling procedure proposed by Breitenberger et al. [15] is based on a penalty approach using so-called B-Rep edge elements to constrain the displacements and rotations to be equal on patch interfaces. It is applied to both trimmed and untrimmed non-conforming Kirchhoff-Love shells. Other examples of coupling non-conforming NURBS patches can be found in [16, 17], where C^0-continuity is enforced for Reissner-Mindlin plates. Dornisch et al. in [16] propose the weak substitution method, a mortar-type technique that expresses the equality of mutual

deformations using a variational equation. This results in a master-slave relationship between the interface variables. In [17] on the other hand, Du et al. employ Nitsche's method, altering the variational formulation to take into account the coupling conditions. Other examples of C^0-coupled non-conforming patches in linear elasticity can be found in [18–22]. Brivadis et al. [18] study mortar methods, while Ruess et al. [19] and Nguyen et al. [20] make use of Nitsche's method. The latter two also study three-dimensional examples (i.e. the coupling of boundary surfaces), and [19] even in combination with an immersed boundary method to treat trimmed NURBS. Apostolatos et al. [21] compare Nitsche's method, a penalty approach and Lagrange multiplier methods for several two-dimensional benchmark cases. Kleiss et al. [22] extend the Finite Element Tearing and Interconnecting approach to isogeometric frameworks, but only treat conforming and hierarchical meshes. Hesch and Betsch [23] apply a mortar method to three-dimensional non-linear elasticity problems.

A disadvantage of these existing techniques is that most of them are either numerically or implementation-wise considerably more demanding as compared to the uncoupled problem. Mortar methods of the type as proposed by Ben Belgacem [24] (based on the saddle point problem using the unconstrained product space), like the work of Brivadis et al. [18], introduce additional variables (typically Lagrange multipliers) to satisfy interface constraints, increasing the system matrix size. Moreover, the choice of the function spaces for these additional variables influences the accuracy of the results. Nitsche's method does not introduce additional Degrees Of Freedom (DOFs), but instead introduces a penalty-like term in the variational formulation for coupling domains. This makes the implementation more involved and the computational costs higher. The effectiveness of this approach can also depend on the appropriate choice of stabilisation parameters. Penalty formulations do not alter the system matrix size either, but they also rely on suitable choices for the penalty factors. In addition, the conditioning of the system matrix can rapidly deteriorate, and the system becomes variationally inconsistent. In this context, the method of Dornisch et al. [16] seems to have some favourable properties: it does not alter the variational formulation and, like other mortar methods leading to the non-conforming positive definite problem as proposed by Bernardi et al. [25], does not introduce additional DOFs. Nonetheless, it still involves the evaluation of variational equations to derive a master-slave relation matrix.

The current work proposes a simple and robust method for patch coupling based on master-slave interface constraints derived from the interface knot vectors. These master-slave relationships only depend on the mesh itself and can therefore be generated in a pre-processing step requiring very limited numerical efforts. This paper will illustrate the accuracy, robustness and versatility of the proposed technique, in particular in comparison to the similar C^0/G^1 method of Lei et al. [14].

The remainder of this text is structured as follows. The next section gives a brief overview of NURBS-based isogeometric analysis. Section 3 then introduces the proposed coupling technique and discusses its features. Section 4 subsequently applies it to different types of problems, for both C^0- and C^1-coupling of multipatch geometries. The paper ends with some concluding remarks.

2. Preliminaries on NURBS-based isogeometric analysis

This section briefly introduces some basic terminology regarding NURBS surfaces and their corresponding basis functions in the context of IGA. A more detailed explanation about IGA can be found in [1, 2] and about NURBS in particular in [26].

NURBS are built up from B-splines. These are defined using a knot vector, which is a sequence of non-decreasing coordinates in the parameter space ξ. Given a polynomial order p and a knot vector $\boldsymbol{\Xi} = [\xi_1, \xi_2, \ldots, \xi_{n+p+1}]$, a set of n (one-dimensional) B-spline basis functions $N_i^p(\xi)$ $(i = 1, \ldots, n)$ can be generated recursively using the Cox – de Boor recursion formula [27, 28]:

$$\begin{aligned} p = 0: \quad & N_i^0(\xi) = \begin{cases} 1 & \xi_i \leq \xi < \xi_{i+1} \\ 0 & \text{otherwise} \end{cases}, \\ p > 0: \quad & N_i^p(\xi) = \frac{\xi - \xi_i}{\xi_{i+p} - \xi_i} N_i^{p-1}(\xi) + \frac{\xi_{i+p+1} - \xi}{\xi_{i+p+1} - \xi_{i+1}} N_{i+1}^{p-1}(\xi). \end{aligned} \tag{1}$$

For a B-spline formed by n basis functions, $n + p + 1$ knots are required: $\xi_k \in \mathbb{R}$ $(k = 1, 2, \ldots, n + p + 1)$. Open knot vectors, where the first and the last knot each have a multiplicity of $p + 1$, are standard in CAD.

To generate a NURBS basis $R_i^p(\xi)$ from these functions, a weight w_i is assigned to every B-spline function $N_i^p(\xi)$:

$$R_i^p(\xi) = \frac{N_i^p(\xi) w_i}{W(\xi)} = \frac{N_i^p(\xi) w_i}{\displaystyle\sum_{i_w=1}^{n} N_{i_w}^p(\xi) w_{i_w}} \quad \text{for } i = 1, \ldots, n, \tag{2}$$

with $W(\xi)$ being the weighting function. Each $R_i^p(\xi)$ is a piecewise rational function, since $N_i^p(\xi)$ and $W(\xi)$ are both piecewise polynomial. If all the weights are equal, then $R_i^p(\xi) = N_i^p(\xi)$: the basis functions are no longer rational and the NURBS degenerates into a B-spline. B-splines are therefore a subset of NURBS. It is worth noting that both B-spline and NURBS bases form partitions of unity. Using a set of vector-valued weighting coefficients $\mathbf{P}_i \in \mathbb{R}^3$ called control points, a linear combination of the basis functions can be obtained to form a NURBS curve $\mathbf{C}(\xi)$:

$$\mathbf{C}(\xi) = \sum_{i=1}^{n} R_i^p(\xi) \mathbf{P}_i. \tag{3}$$

Multivariate NURBS entities are generated by taking the tensor product of univariate NURBS bases. Given two polynomial orders p and q, and a pair of knot vectors $\boldsymbol{\Xi} = [\xi_1, \xi_2, \ldots, \xi_{n+p+1}]$ and $\boldsymbol{H} = [\eta_1, \eta_2, \ldots, \eta_{m+q+1}]$, a bivariate NURBS basis is defined as

$$R_{i,j}^{p,q}(\xi, \eta) = \frac{N_i^p(\xi) M_j^q(\eta) w_{i,j}}{\displaystyle\sum_{i_w=1}^{n} \sum_{j_w=1}^{m} N_{i_w}^p(\xi) M_{j_w}^q(\eta) w_{i_w, j_w}} \quad \text{for } \begin{matrix} i = 1, \ldots, n \\ j = 1, \ldots, m, \end{matrix} \tag{4}$$

where $N_i^p(\xi)$ and $M_j^q(\eta)$ represent univariate B-spline basis functions of order p and q, associated with knot vectors $\boldsymbol{\Xi}$ and $\boldsymbol{H}$, respectively. A NURBS surface geometry $\boldsymbol{S}(\xi, \eta)$ is then defined in analogy with a NURBS curve using a net of control points $\mathbf{P}_{i,j} \in \mathbb{R}^3$:

$$\mathbf{S}(\xi, \eta) = \sum_{i=1}^{n} \sum_{j=1}^{m} R_{i,j}^{p,q}(\xi, \eta) \mathbf{P}_{i,j}. \tag{5}$$

It should be noted that the control points are in general not interpolatory, i.e. they do not necessarily lie on the surface they define.

Applying the isoparametric paradigm, a NURBS basis can be used in shape function expansions to approximate field variables. Taking $u(\xi, \eta)$ to represent the primary variable, its approximation $\hat{u}(\xi, \eta)$ then becomes:

$$u(\xi,\eta) \approx \hat{u}(\xi,\eta) = \sum_{i=1}^{n}\sum_{j=1}^{m} R_{i,j}^{p,q}(\xi,\eta)\cdot d_{i,j} = \sum_{k=1}^{n\cdot m} R_{k}^{p,q}(\xi,\eta)\cdot d_{k}, \tag{6}$$

where d_k are the unknown control variables to be solved for, with $k = i + (j-1)\cdot m$ a single counter replacing i and j. Using a Galerkin approach, these same shape functions are then also used as test functions in a weighted residual formulation.

Equation (5) represents a single NURBS surface patch. A general NURBS surface typically consists of a combination of several patches. Each patch is a concatenation of knot spans. These are delimited by (non-identical) knots and represent the elements in the mesh, where the basis functions are smooth (i.e. C^∞-continuous). Across a knot ξ_i, the basis functions have a C^{p-m_i}-continuity, with m_i being the multiplicity of knot ξ_i. NURBS bases are therefore quite flexible regarding inter-element continuity: virtually arbitrarily high continuities can be obtained. Across patch boundaries, however, the discretisation is by default discontinuous, and care needs to be taken to ensure that the field variable space maintains the necessary continuity. This is trivial in the case of enforcing C^0-continuity across patches with matching discretisations, but cannot be done straightforwardly or even exactly in a more general case. Ensuring coupling across patch boundaries in a robust and flexible manner is the subject of this paper; the proposed approach is explained in detail in the following section.

3. Patch coupling using a master-slave relationship based on virtual uncommon knot-insertion

The proposed technique couples patches by making use of fundamental relationships between the basis functions of a NURBS curve and those of a knot-inserted version of it. They are the same relationships as used in e.g. Bézier extraction [29]. The underlying idea behind the proposed method was inspired by a study by Cottrell et al. [9] where a special case of this technique is applied to hierarchical NURBS meshes, building upon the approach of Kagan et al. [30] for hierarchical B-splines. The approach proposed in the current manuscript is comparable to the C^0/G^1 coupling method presented by Lei et al. [14], although both techniques differ fundamentally. The continuity constraints are derived in a similar manner, but result in different coupling equations. Moreover, Lei et al. suggest to satisfy the interface constraints by means of a penalty formulation, whereas the method proposed here employs a substitution technique based on master-slave relationships. These differences are crucial to ensure the accuracy of the coupling, as will be illustrated in the numerical examples in section 4. The rest of the current section first presents the derivation of the proposed coupling equations, and then how they are taken into account when solving the global system of equations.

3.1. Generating the interface constraints

The basic coupling procedure is explained here for the case of two patches, but the next section mentions how to take into account an arbitrary number of interfaces. The procedure is presented for C^0-coupling, but can be extended to higher-order continuities. The control variables of the slave patch are expressed in function of the master patch. The patch with the finer discretisation on the interface is taken to be the slave, and the

coarser one the master. This choice provides the most flexibility to comply with the interface constraints, as will be explained in more detail further on in the text. In what follows, quantities pertaining to the master and the slave are denoted by subscripts 'm' and 's', respectively, or 'α' when referring to either one.

Consider two non-conforming patches of the same polynomial order p. The latter is a prerequisite for the proposed method, otherwise the coupling relationships derived in this section do not hold (in which case a straightforward workaround could be to first degree-elevate the lower-order patch until its order matches that of the other one). The top left illustration of fig. 1 presents the uncoupled patch configuration. Black lines represent the patch boundaries, grey lines the mesh. The left and right patch are the slave and the master, respectively. Their interface control points $\mathbf{d}_\mathrm{s}$ and $\mathbf{d}_\mathrm{m}$ are indicated by circles and squares, respectively. If both interface discretisations were identical, coupling would be trivial by means of a one-to-one matching of these interface DOFs. But since this is not the case, the patches are virtually refined until they are conforming. This is done by inserting into both interface knot vectors the knots that are present in the other patch's knot vector, but not in that of the patch itself (taking into account knot multiplicities). That is: given the two interface knot vectors $\boldsymbol{\Xi}_\mathrm{m}$ and $\boldsymbol{\Xi}_\mathrm{s}$, refine them until they are both identical to $\boldsymbol{\Xi}_{\mathrm{m}\cup\mathrm{s}} = \boldsymbol{\Xi}_\mathrm{m} \cup \boldsymbol{\Xi}_\mathrm{s}$. The top right part of fig. 1 illustrates this, with the resulting control variables $\mathbf{d}_\alpha^v$ after refinement indicated by the solid triangles. This refinement process is referred to here as *virtual uncommon knot insertion*. It is virtual in the sense that these finer discretisations are never used for shape function expansions; only the coupling equations resulting from a one-to-one matching of the refined control variables $\mathbf{d}_\alpha^v$ are used to link the original control variables $\mathbf{d}_\alpha$ on the interface.

Let $\overline{\boldsymbol{\Xi}}_\alpha = \boldsymbol{\Xi}_{\mathrm{m}\cup\mathrm{s}} \setminus \boldsymbol{\Xi}_\alpha = \{\bar{\xi}_{1,\alpha}, \ldots, \bar{\xi}_{r_\alpha,\alpha}\}$ be the set of r_α knots that need to be inserted into $\boldsymbol{\Xi}_\alpha = \{\xi_{1,\alpha}, \ldots, \xi_{n_\alpha+p+1,\alpha}\}$ (for $\alpha = \mathrm{m}, \mathrm{s}$). Very similar to using Bézier extraction operators [29], the set $\mathbf{P}_\alpha^v = [\mathbf{P}_{1,\alpha}^v, \ldots, \mathbf{P}_{n_\alpha+r_\alpha,\alpha}^v]^T$ of the $n_\alpha + r_\alpha$ control points of the refined version can be determined from the n_α original ones $\mathbf{P}_\alpha = [\mathbf{P}_{1,\alpha}, \ldots, \mathbf{P}_{n_\alpha,\alpha}]^T$ using virtual refinement operators A_α:

$$\begin{aligned} \mathbf{P}_\alpha^v &= \mathsf{A}_\alpha \mathbf{P}_\alpha \\ &= (\mathsf{W}_\alpha^v)^{-1} \mathsf{B}_\alpha \mathsf{W}_\alpha \mathbf{P}_\alpha, \end{aligned} \tag{7}$$

where B_α can be calculated using only the original interface knots and the ones to be inserted. In particular, B_α is the product of separate matrix operators $\mathsf{B}_\alpha^{(j_\alpha)}$ representing the subsequent insertions of each additional knot $\bar{\xi}_{j_\alpha}$. It is given by $\mathsf{B}_\alpha = \mathsf{B}_\alpha^{(1)} \mathsf{B}_\alpha^{(2)} \cdots \mathsf{B}_\alpha^{(r_\alpha-1)} \mathsf{B}_\alpha^{(r_\alpha)}$, with

$$\mathsf{B}_\alpha^{(j_\alpha)} = \begin{bmatrix} \lambda_1^{(j_\alpha)} & 0 & & \cdots & & & 0 \\ 1-\lambda_2^{(j_\alpha)} & \lambda_2^{(j_\alpha)} & 0 & & \cdots & & 0 \\ 0 & 1-\lambda_3^{(j_\alpha)} & \lambda_3^{(j_\alpha)} & 0 & & \cdots & 0 \\ \vdots & & & \ddots & & & \vdots \\ 0 & \cdots & & & 0 & 1-\lambda_{n_\alpha+j_\alpha-1}^{(j_\alpha)} & \lambda_{n_\alpha+j_\alpha-1}^{(j_\alpha)} \\ 0 & & \cdots & & & 0 & 1-\lambda_{n_\alpha+j_\alpha}^{(j_\alpha)} \end{bmatrix}, \tag{8}$$

with

$$\lambda_i^{(j_\alpha)} = \begin{cases} 1 & i \leq k^{(j_\alpha)} - p \\ \dfrac{\bar{\xi}_{j_\alpha,\alpha} - \xi_{i,\alpha}}{\xi_{i+p,\alpha} - \xi_{i,\alpha}} & k^{(j_\alpha)} - p + 1 \leq i \leq k^{(j_\alpha)} \\ 0 & i \geq k^{(j_\alpha)} + 1 \end{cases} \quad \text{for} \quad \begin{matrix} i & = 1, \ldots, n_\alpha + j_\alpha \\ j_\alpha & = 1, \ldots, r_\alpha \end{matrix}, \tag{9}$$

where the knot index $k^{(j_\alpha)}$ can be found from the value of the inserted knot $\bar{\xi}_{j_\alpha,\alpha}$, i.e. $\bar{\xi}_{j_\alpha,\alpha} \in [\xi_{k^{(j_\alpha)},\alpha}, \xi_{k^{(j_\alpha)}+1,\alpha}[$. The matrices W_α and W_α^v are diagonal matrices containing the NURBS weights (cf. eq. (2)) for the original basis functions and the virtually refined ones, respectively. Their diagonals are given by $\mathbf{w}_\alpha = \{w_{1,\alpha}, \ldots, w_{n_\alpha,\alpha}\}^T$ and $\mathbf{w}_\alpha^v = \{w_{1,\alpha}^v, \ldots, w_{n_\alpha+r_\alpha,\alpha}^v\}^T = \mathsf{B}_\alpha \mathbf{w}_\alpha$, respectively:

$$\mathsf{W}_\alpha = \begin{bmatrix} w_{1,\alpha} & & & \\ & w_{2,\alpha} & & \\ & & \ddots & \\ & & & w_{n_\alpha,\alpha} \end{bmatrix} \qquad \mathsf{W}_\alpha^v = \begin{bmatrix} w_{1,\alpha}^v & & & \\ & w_{2,\alpha}^v & & \\ & & \ddots & \\ & & & w_{n_\alpha+r_\alpha,\alpha}^v \end{bmatrix}. \tag{10}$$

Both A_α and B_α have dimensions $(n_\alpha + r_\alpha) \times n_\alpha$. In the case of B-splines, A_α is identical to B_α.

The relationship in eq. (7) is expressed for control points of the virtually refined interface curves, but it can also be used for the vectors of interface control variables $\mathbf{d}_\alpha$ and $\mathbf{d}_\alpha^v$:

$$\mathbf{d}_\alpha^v = \mathsf{A}_\alpha \mathbf{d}_\alpha \qquad \alpha = \mathrm{m}, \mathrm{s}. \tag{11}$$

The extraction operators A_m and A_s now link the original interface control variables $\mathbf{d}_\mathrm{m}$ and $\mathbf{d}_\mathrm{s}$ to the control variables $\mathbf{d}_\mathrm{m}^v$ and $\mathbf{d}_\mathrm{s}^v$ of the virtually refined versions. In other words, the matrix operators $\mathsf{A}_\alpha = (\mathsf{W}_\alpha^v)^{-1} \mathsf{B}_\alpha \mathsf{W}_\alpha$ express the linear combinations of the original control points that result in each refined control point. At first sight, continuity then requires $\mathbf{d}_\mathrm{m}^v = \mathbf{d}_\mathrm{s}^v$, yielding the following interface constraints:

$$\mathsf{A}_\mathrm{m} \mathbf{d}_\mathrm{m} - \mathsf{A}_\mathrm{s} \mathbf{d}_\mathrm{s} = \mathbf{0}. \tag{12}$$

Enforcing these constraints works well in the case of hierarchical meshes, where they lead to an exact coupling (as already illustrated by Cottrell et al. in [9]). However, in an arbitrary patch configuration, these equations can overconstrain the system and lead to inaccurate and non-converging solutions. The numerical examples in section 4 demonstrate this. To cope with that potential conflict, the present work proposes to use a master-slave formulation, leading to the following continuity relationships:

$$\mathbf{d}_\mathrm{s} = \mathsf{A}_\mathrm{s}^+ \mathsf{A}_\mathrm{m} \mathbf{d}_\mathrm{m} = \mathsf{T}_\mathrm{sm} \mathbf{d}_\mathrm{m}, \tag{13}$$

with A_s^+ the Moore-Penrose pseudo-inverse of A_s. This is equivalent to approximating the (virtually refined) master functions using the slave functions in a least-squares sense, given the interface constraints from eq. (12). The slave is chosen to be the more finely discretised patch. This means that the coupling matrix $\mathsf{T}_\mathrm{sm} = \mathsf{A}_\mathrm{s}^+ \mathsf{A}_\mathrm{m}$ has dimensions $n_\mathrm{s} \times n_\mathrm{m}$ with $n_\mathrm{m} \leq n_\mathrm{s}$, where n_m and n_s are the number of interface variables in the master and slave patch, respectively. The reasoning behind this choice is that possibly conflicting constraints can then be (approximately) satisfied with the least amount of independent (and thus possibly interfering) variables. By using more slave DOFs to accommodate the coupling requirements to match a smaller number of master DOFs, the

mismatch between both discretisations on the interface is kept to a minimum. This choice leads to an exact continuity enforcement for hierarchical patches [9], whereas this is not guaranteed if the more refined patch is taken to be the master.

Figure 1 summarises the presented coupling procedure. The top left part shows the uncoupled, non-conforming patches, which are then made conforming by virtually refining them. This leads to the configuration in the top right, where $\mathbf{d}_{\mathrm{m}}^{v} = \mathbf{d}_{\mathrm{s}}^{v}$ has to hold. The bottom part of the figure represents the coupled patches, with only $\mathbf{d}_{\mathrm{m}}$ as remaining interface DOFs, but with $\mathbf{d}_{\mathrm{s}}$ and $\mathbf{d}_{\mathrm{m}}$ still linked by eq. (13). By using a substitution method for condensation of the slave DOFs $\mathbf{d}_{\mathrm{s}}$ according to eq. (13), the global system of equations can then be solved while taking into account the continuity conditions. This is explained in more detail in the following section. The proposed coupling approach properly satisfies the continuity requirements, without overconstraining the original system of equations. The rest of the text refers to it as *Virtual Uncommon-Knot-Inserted Master-Slave* (VUKIMS) coupling, since it enforces a master-slave relationship based on constraints derived using virtual uncommon knot insertion.

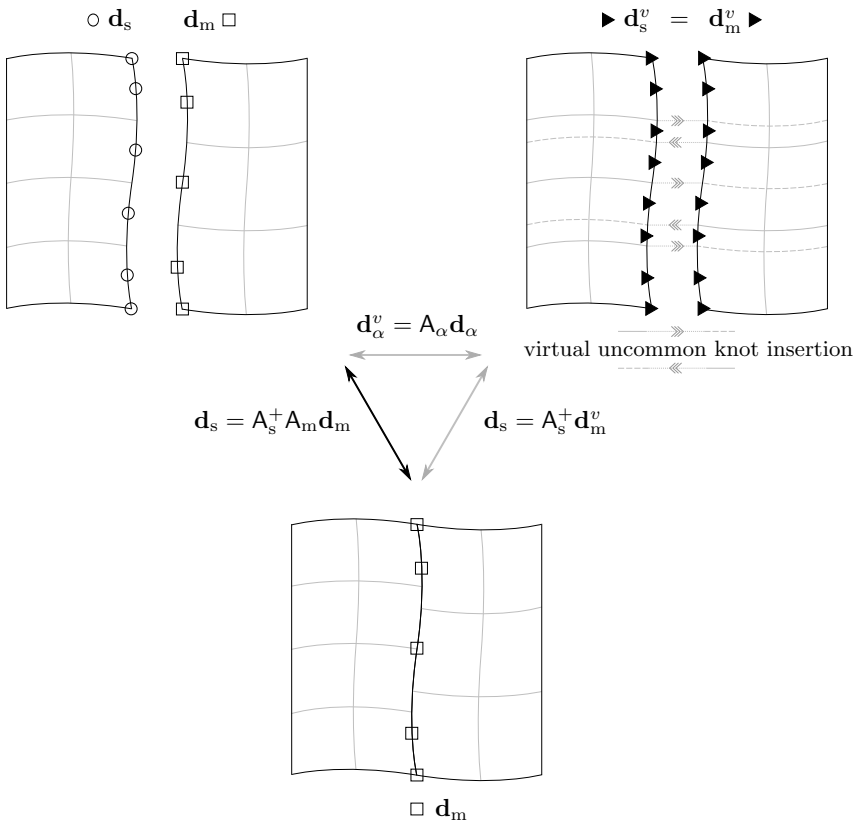

Figure 1: Conceptual illustration of the patch coupling method. Using restrictions resulting from the matching of (virtually) uncommon knot-inserted meshes (top right) that are transformed back to the original control variables (top left), C^0-continuity conditions can be (weakly) enforced within a master-slave relationship (bottom), only retaining the master DOFs. The right patch is the less refined one and therefore the master.

3.2. Taking into account the interface constraints

Consider a general multipatch geometry which consists of an arbitrary number of NURBS patches and accompanying interfaces. For each of these n_{int} interfaces, the corresponding DOFs can be linked by a master-slave relationship as in eq. (13):

$$\mathbf{d}_{\text{s}}^{(i)} = \mathsf{T}_{\text{sm}}^{(i)} \mathbf{d}_{\text{m}}^{(i)} \qquad \text{for} \quad i = 1, \ldots, n_{\text{int}}. \tag{14}$$

Let $\mathbf{u}_{\text{M}} = \cup_{i=1}^{n_{\text{int}}} \mathbf{d}_{\text{m}}^{(i)}$ be the union of all the resulting master DOFs, and $\mathbf{u}_{\text{S}} = \cup_{i=1}^{n_{\text{int}}} \mathbf{d}_{\text{s}}^{(i)}$ that of all the slave DOFs. All of the interface constraints from eq. (14) can then be collected into a single matrix T_{SM} such that:

$$\mathbf{u}_{\text{S}} = \mathsf{T}_{\text{SM}} \mathbf{u}_{\text{M}}, \tag{15}$$

where T_{SM} contains zeros, except at the entries describing the constraints:

$$\mathsf{T}_{\text{SM}}(\mathbf{i}_{\text{s}}^{(i)}, \mathbf{i}_{\text{m}}^{(i)}) = \mathsf{T}_{\text{sm}}^{(i)} \qquad \text{with} \qquad \begin{aligned} \mathbf{u}_{\text{S}}(\mathbf{i}_{\text{s}}^{(i)}) &= \mathbf{d}_{\text{s}}^{(i)} \\ \mathbf{u}_{\text{M}}(\mathbf{i}_{\text{m}}^{(i)}) &= \mathbf{d}_{\text{m}}^{(i)} \end{aligned} \qquad \text{for} \quad i = 1, \ldots, n_{\text{int}}. \tag{16}$$

In other words, the constraints matrix T_{SM} gives the dependencies of all the slave DOFs on all the master DOFs, taking into account all interfaces. These constraints, however, are not linearly independent in a general patch configuration. Circular dependencies can be introduced at points where multiple interfaces meet, and some interface DOFs might act as both a master and a slave. The constraints are therefore rewritten in homogeneous form:

$$\mathsf{T}_{\text{SM}} \mathbf{u}_{\text{M}} - \mathbf{u}_{\text{S}} = \mathbf{0}. \tag{17}$$

Or, expressing this using a single constraints matrix R_{SM}:

$$\mathsf{R}_{\text{SM}} \mathbf{u}_{\text{MS}} = \mathbf{0} \qquad \text{with} \quad \mathbf{u}_{\text{MS}} = \mathbf{u}_{\text{M}} \cup \mathbf{u}_{\text{S}}. \tag{18}$$

From this matrix, the linearly independent constraint equations (i.e. the linearly independent rows) need to be extracted. This can be done for instance by computing the rank-revealing QR factorisation of the transpose of R_{SM} [31]. The resulting linearly independent rows of R_{SM} are collected in the reduced constraints matrix $\mathsf{R}_{\text{SM,LI}}$. Using this matrix of size $n_{\text{D}} \times (n_{\text{D}} + n_{\text{I}})$ and starting from the original slave DOFs $\mathbf{u}_{\text{S}}$, a set of n_{D} dependent interface DOFs $\mathbf{u}_{\text{D}}$ can be selected; the n_{I} independent interface DOFs $\mathbf{u}_{\text{I}}$ are then given by $\mathbf{u}_{\text{I}} = \mathbf{u}_{\text{MS}} \setminus \mathbf{u}_{\text{D}}$. To transform $\mathsf{R}_{\text{SM,LI}}$ to an equivalent system of equations that is more convenient for enforcing the coupling constraints, Gaussian elimination is applied to it using the dependent DOFs $\mathbf{u}_{\text{D}}$ as pivots (such that in the end each row contains only a single non-zero entry for the dependent DOFs). The resulting matrix R_{DI} still represents the original constraints as in eq. (18): $\mathsf{R}_{\text{DI}} \mathbf{u}_{\text{MS}} = \mathbf{0}$ is equivalent to $\mathsf{R}_{\text{SM}} \mathbf{u}_{\text{MS}} = \mathbf{0}$. Without loss of generality, the interface DOFs can be ordered in such a way that $\mathbf{u}_{\text{MS}} = \begin{Bmatrix} \mathbf{u}_{\text{D}}^T & \mathbf{u}_{\text{I}}^T \end{Bmatrix}^T$. The modified constraints matrix R_{DI} can then be written as $\mathsf{R}_{\text{DI}} = \begin{bmatrix} \mathsf{I}_{n_{\text{D}} \times n_{\text{D}}} & -\mathsf{T}_{\text{DI}} \end{bmatrix}$, where $\mathsf{I}_{n_{\text{D}} \times n_{\text{D}}}$ is the identity matrix of size n_{D}, and T_{DI} the substitution matrix expressing the relationship between $\mathbf{u}_{\text{D}}$ and $\mathbf{u}_{\text{I}}$ that enforces the interface coupling:

$$\mathbf{u}_{\text{D}} = \mathsf{T}_{\text{DI}} \mathbf{u}_{\text{I}}. \tag{19}$$

Note that this procedure to obtain R_{DI} is equivalent to computing the reduced row echelon form of R_{SM} (given the proper ordering of the DOFs as mentioned above) and retaining only the non-zero rows.

Consider now the global system of equations to be solved: $\mathsf{K}\mathbf{u} = \mathbf{f}$, with K the system matrix, $\mathbf{u}$ the vector of unknowns, and $\mathbf{f}$ the force vector. The (column) vector of unknowns $\mathbf{u}$ can be split into three groups: $\mathbf{u} = \begin{Bmatrix}\mathbf{u}_\mathrm{O}^T & \mathbf{u}_\mathrm{I}^T & \mathbf{u}_\mathrm{D}^T\end{Bmatrix}^T$, with $\mathbf{u}_\mathrm{O}$ the n_O DOFs not belonging to any interface, and $\mathbf{u}_\mathrm{I}$ and $\mathbf{u}_\mathrm{D}$ as defined above. The system matrix and force vector are also partitioned accordingly:

$$\mathsf{K} = \begin{bmatrix} \mathsf{K}_{\mathrm{OO}} & \mathsf{K}_{\mathrm{OI}} & \mathsf{K}_{\mathrm{OD}} \\ \mathsf{K}_{\mathrm{IO}} & \mathsf{K}_{\mathrm{II}} & \mathsf{K}_{\mathrm{ID}} \\ \mathsf{K}_{\mathrm{DO}} & \mathsf{K}_{\mathrm{DI}} & \mathsf{K}_{\mathrm{DD}} \end{bmatrix} \qquad \mathbf{u} = \begin{Bmatrix} \mathbf{u}_\mathrm{O} \\ \mathbf{u}_\mathrm{I} \\ \mathbf{u}_\mathrm{D} \end{Bmatrix} \qquad \mathbf{f} = \begin{Bmatrix} \mathbf{f}_\mathrm{O} \\ \mathbf{f}_\mathrm{I} \\ \mathbf{f}_\mathrm{D} \end{Bmatrix}. \tag{20}$$

By applying the substitution from eq. (19) (for both the test and the trial functions), a reduced system of equations is obtained: $\mathsf{K}_\mathrm{r}\mathbf{u}_\mathrm{r} = \mathbf{f}_\mathrm{r}$, where

$$\mathsf{K}_\mathrm{r} = \begin{bmatrix} \mathsf{K}_{\mathrm{OO}} & \mathsf{K}_{\mathrm{OI}} + \mathsf{K}_{\mathrm{OD}}\mathsf{T}_{\mathrm{DI}} \\ \mathsf{K}_{\mathrm{IO}} + \mathsf{T}_{\mathrm{DI}}^T\mathsf{K}_{\mathrm{DO}} & \mathsf{K}_{\mathrm{II}} + \mathsf{K}_{\mathrm{ID}}\mathsf{T}_{\mathrm{DI}} + \mathsf{T}_{\mathrm{DI}}^T(\mathsf{K}_{\mathrm{DI}} + \mathsf{K}_{\mathrm{DD}}\mathsf{T}_{\mathrm{DI}}) \end{bmatrix} \quad \mathbf{u}_\mathrm{r} = \begin{Bmatrix} \mathbf{u}_\mathrm{O} \\ \mathbf{u}_\mathrm{I} \end{Bmatrix} \quad \mathbf{f}_\mathrm{r} = \begin{Bmatrix} \mathbf{f}_\mathrm{O} \\ \mathbf{f}_\mathrm{I} + \mathsf{T}_{\mathrm{DI}}^T\mathbf{f}_\mathrm{D} \end{Bmatrix}. \tag{21}$$

The final number of DOFs to be solved for is now $n_\mathrm{O} + n_\mathrm{I}$, a reduction of n_D with respect to the original system. The dependent DOFs $\mathbf{u}_\mathrm{D}$ are computed after solving this reduced system of equations by resubstituting the resulting independent DOFs $\mathbf{u}_\mathrm{I}$ in eq. (19). It is worth noting that in the case of a single interface there are no linearly dependent interface constraints, and T_DI is identical to T_sm from eq. (13).

3.3. Enforcing C^1-continuity

The derivation above was given for C^0-coupling, but the same approach can be used for enforcing higher-order continuities. The precise equations are different — as higher-order-continuity is influenced by several rows of control points near the interface — but the VUKIMS concept can still be used in very much the same way. Section 4.2 demonstrates this for two examples of C^1-coupling in a multipatch Kirchhoff-Love shell formulation.

The C^1-continuity depends on the shape functions' first-order derivatives normal to patch interfaces. They can be coupled by demanding that the control variables (of the virtually refined configuration) right next to the interface on either side of it be collinear with those on the interface. This collinearity of control variables has already been successfully used for the coupling of conforming NURBS patches of Kirchhoff-Love shells in [10]. It is a valid approach only if the bordering patches' mesh lines that touch the interface meet parallelly, otherwise the shape function derivatives are not coupled in the correct (identical) physical direction. Nonetheless, the collinearity enforcement is useful as a validation and benchmarking tool for coupling methods in a higher-order continuity setting.

Consider again a single interface configuration. Let $\mathbf{d}_{\alpha 1}$ be the interface control variables and $\mathbf{d}_{\alpha 2}$ the control variables adjacent to the interface. Equation (12) for C^0-continuity then becomes $\mathsf{A}_{\mathrm{m}1}\mathbf{d}_{\mathrm{m}1} = \mathsf{A}_{\mathrm{s}1}\mathbf{d}_{\mathrm{s}1}$, and imposing collinearity of the control points for the virtually refined configuration results in:

$$\mathsf{A}_{\mathrm{s}1}\mathbf{d}_{\mathrm{s}1} - \mathsf{A}_{\mathrm{s}2}\mathbf{d}_{\mathrm{s}2} = \mathsf{C}_{\mathrm{sm}}\left(\mathsf{A}_{\mathrm{m}2}\mathbf{d}_{\mathrm{m}2} - \mathsf{A}_{\mathrm{m}1}\mathbf{d}_{\mathrm{m}1}\right), \tag{22}$$

where C_{sm} is a diagonal matrix containing mesh-dependent constants for the collinearity expression. Together with the previously derived C^0 interface constraints, these equations express the C^1 coupling conditions. Transforming these equations back to the original

configuration using the master-slave approach then yields the following C^1-continuity relationships:

$$\mathbf{d}_{s1} = \mathsf{A}_{s1}^{+}\mathsf{A}_{m1}\mathbf{d}_{m1}, \tag{23a}$$

$$\mathbf{d}_{s2} = \mathsf{A}_{s2}^{+}\left[\mathsf{A}_{s1}\mathbf{d}_{s1} - \mathsf{C}_{sm}\left(\mathsf{A}_{m2}\mathbf{d}_{m2} - \mathsf{A}_{m1}\mathbf{d}_{m1}\right)\right]. \tag{23b}$$

By using eq. (23a), the C^0 slave variables $\mathbf{d}_{s1}$ can be eliminated from eq. (23b). Similarly to eq. (13) for the purely C^0 case, the C^1-continuity conditions can then be expressed using coupling matrices $\mathsf{T}_{s\bullet m\star}$ between the master and slave variables as follows:

$$\begin{cases} \mathbf{d}_{s1} = \mathsf{A}_{s1}^{+}\mathsf{A}_{m1}\mathbf{d}_{m1} = \mathsf{T}_{s1m1}\mathbf{d}_{m1} \\ \mathbf{d}_{s2} = \mathsf{A}_{s2}^{+}\left(\mathsf{A}_{s1}\mathsf{A}_{s1}^{+} + \mathsf{C}_{sm}\right)\mathsf{A}_{m1}\mathbf{d}_{m1} - \mathsf{A}_{s2}^{+}\mathsf{C}_{sm}\mathsf{A}_{m2}\mathbf{d}_{m2} = \mathsf{T}_{s2m1}\mathbf{d}_{m1} + \mathsf{T}_{s2m2}\mathbf{d}_{m2} \end{cases}. \tag{24}$$

Note that $\mathsf{A}_{s1}\mathsf{A}_{s1}^{+}$ is in general not equal to the identity matrix (but $\mathsf{A}_{s1}^{+}\mathsf{A}_{s1}$ is since A_{s1} is of full column rank). This set of equations (or multiple sets in the case of multiple interfaces) can now be taken into account in the same way as explained in the previous section, by determining a set of independent equations and substituting the dependent DOFs. The extraction operators $\mathsf{A}_{\alpha 1}$ and $\mathsf{A}_{\alpha 2}$ can be computed as in eqs. (7) to (10), but using the NURBS weights of the basis functions adjacent to the interface for $\mathsf{A}_{\alpha 2}$. If B-splines are used, all weights are equal and $\mathsf{A}_{\alpha 1} = \mathsf{A}_{\alpha 2}$.

3.4. Some patch coupling considerations

The main merit of the VUKIMS coupling lies in its simplicity and flexibility. The coupling relationships in eq. (19) are linear and they are established using only the interface knot vectors (and NURBS weights in the case of NURBS), in a straightforward and inexpensive pre-processing step. No assumptions are required with regard to patch conformity; the method is valid for both conforming and non-conforming interfaces — in the case of conforming patches the method reduces to a one-to-one matching of the interface variables. Once computed, the interface constraints can be enforced through simple matrix condensation (even reducing the model size). These steps are all independent of any problem-specific parameters, and as such, the VUKIMS coupling operates on a mathematical level and not on a physical one. This makes it very versatile with respect to the variety of different problem types it can handle, like other techniques that employ matrix condensation for incorporating coupling constraints, such as the mortar method proposed by Bernardi et al. [25].

The numerical examples in the next section are used to validate the proposed VUKIMS patch coupling and demonstrate its robustness. Moreover, it is compared to the C^0/G^1 method developed by Lei et al. [14]. That method also uses virtual uncommon knot insertion to obtain virtual matching meshes, but it directly enforces eq. (12) and/or (22) instead of using a master-slave formulation. In the case of hierarchical meshes, both methods are equivalent and reduce to the technique developed by Cottrell et al. [9], leading to an exact continuity enforcement. In fact, the C^0/G^1 method always leads to the continuity being exactly satisfied, but it does not in general converge to the correct solution. This is because arbitrary non-conformities can quickly lead to the interface being overconstrained. The proposed VUKIMS coupling relaxes this overconstraining in a least-squares sense by using the master-slave formulation given by eq. (13). The numerical examples in the section below demonstrate the accuracy and robustness of this approach.

4. Numerical examples

This section applies the proposed VUKIMS coupling technique to several problem types. The first part demonstrates a C^0-coupling for Helmholtz problems, both in a two-dimensional finite element setting and in a three-dimensional boundary element formulation. Section 4.2 then applies a C^1-coupling to Kirchhoff-Love shell structures. All simulations in this work are isogeometric simulations. They are carried out using in-house MATLAB code that uses some functionalities from the open-source frameworks GeoPDEs [32] and IGAFEM [3].

4.1. C^0-coupling: 2D and 3D Helmholtz problems

This part first analyses the Helmholtz eigenvalue problem, studying the accuracy of both the eigenfrequencies and eigenmodes. Sections 4.1.2 and 4.1.3 then solve two acoustic boundary value problems. More information about the use of isogeometric approaches for solving acoustic problems can be found in a.o. [33–35].

4.1.1. Eigenvalue problem for a square domain.

Consider a unit square domain governed by the Helmholtz equation and with Neumann boundary conditions (e.g. an acoustic cavity with rigid boundaries). Assuming unit material properties, the eigenfrequencies can be found by solving the following problem for ω:

$$\begin{aligned} &\boldsymbol{\nabla}^2 u(x,y) + \omega^2 u(x,y) = 0, \qquad (x,y) \in V = [0,1]\,\mathrm{m} \times [0,1]\,\mathrm{m}, \\ &\frac{\partial u}{\partial n}(x,y)\Big|_{\partial V} = 0, \end{aligned} \tag{25}$$

with $\boldsymbol{\nabla}^2 \bullet = \frac{\partial^2 \bullet}{\partial x^2} + \frac{\partial^2 \bullet}{\partial y^2}$ the Laplacian and $\frac{\partial \bullet}{\partial n}$ the normal derivative operator. The solution for this problem can be analytically calculated [36] and yields the following description for the exact eigenfrequencies $\omega_{mn,\mathrm{ex}}$ and mode shapes $u_{mn,\mathrm{ex}}$:

$$\omega_{mn,\mathrm{ex}} = \pi\sqrt{m^2+n^2}, \qquad m,n = 0,1,2,\ldots, \tag{26}$$

$$u_{mn,\mathrm{ex}}(x,y) = \cos(m\pi x)\cos(n\pi y), \qquad m,n = 0,1,2,\ldots. \tag{27}$$

The problem is numerically solved using a single patch model and using meshes which consist of four equally-sized, non-conforming, non-hierarchical patches. Figure 2 shows the topologies for these models. The single patch and four-patch model contain 64 and 68 elements, respectively, but they are built using different sets of basis functions. When

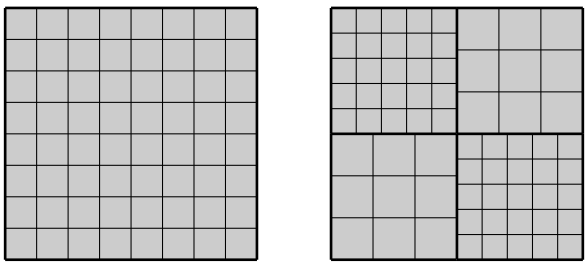

(a) Single patch. (b) Four patches.

Figure 2: The single patch and multipatch base meshes used to solve the Helmholtz eigenvalue problem. The thicker lines are the patch boundaries.

using quadratic B-splines, the single patch mesh contains 99 DOFs, while the four-patch model has 148 uncoupled DOFs. After applying the VUKIMS coupling, this number is reduced to 121. For analysing the four-patch configuration, the proposed VUKIMS coupling method is compared to the C^0/G^1 method with static condensation (C^0/G^1SC). This allows evaluating the accuracy of enforcing eq. (13) (VUKIMS) versus eq. (12) (C^0/G^1) as interface constraints. The single patch model (fig. 2a) is denoted as 'SP', while all other models refer to the four-patch topology (fig. 2b). All meshes in this section consist of biquadratic B-splines. The convergence behaviour is studied using a series of refined meshes, starting from the ones in fig. 2. For the four-patch meshes, the original difference in the number of elements across interfaces is maintained between different refinement steps (as opposed to the original ratio of these numbers). This means that these meshes always remain non-conforming (and non-hierarchical), but that the mesh size becomes more uniform after refinement.

Consider the first non-zero eigenfrequency, i.e. the double eigenfrequency $\omega_{01,\mathrm{ex}} = \omega_{10,\mathrm{ex}} = \pi$ (cf. eq. (26)). Figure 3a shows the convergence of the relative error of this eigenfrequency versus the average element size h, starting from the meshes in fig. 2. All three methods yield an accurate value, with errors well below 0.1 %. However, the four-patch model with the C^0/G^1SC method does not converge, not even for this first eigenfrequency. The VUKIMS coupling on the other hand, does show a decreasing error with decreasing mesh size, as does the single patch model. The VUKIMS model exhibits a larger error than the single patch case, which is partly due to the less uniform mesh size. This observation can also be made for higher eigenfrequencies. Figure 3b shows the relative eigenfrequency error for the lower half of the normalised frequency spectrum i/N (with i the mode number and N the total number of DOFs), calculated with around

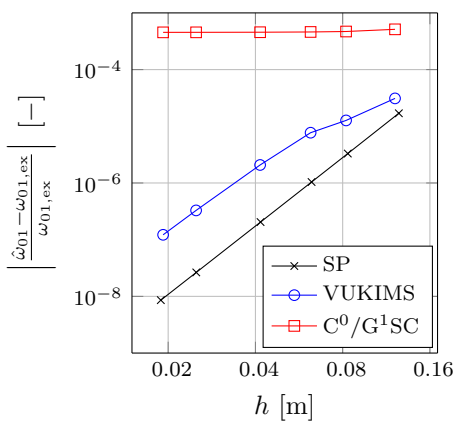

(a) Convergence of the first non-zero eigenfrequency versus the average element size. While the VUKIMS coupling follows the single patch model well, the C^0/G^1 approach stagnates at an accuracy of $5{\cdot}10^{-4}$.

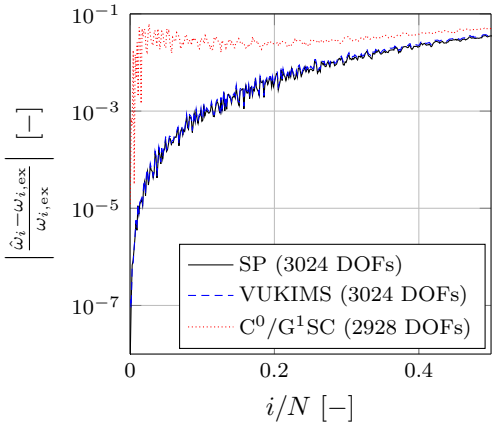

(b) Relative error of the lower half of the eigenfrequencies versus the normalised mode number (using models of about 3000 quadratic DOFs). The VUKIMS coupling delivers nearly identical performance as the single patch model.

Figure 3: Assessment of the accuracy of the numerical eigenfrequencies $\hat{\omega}_i$ of the unit square, calculated for the different models using quadratic B-spline basis functions, based on the meshes in fig. 2.

3000 DOFs (corresponding to an average element size h of about 0.019 m). For the C^0/G^1SC coupling, the eigenfrequency accuracy rapidly deteriorates with increasing mode number: only the lower 5 % of the modes have an eigenfrequency error below 1 %. The VUKIMS model yields the same accuracy as the single patch model, with the first 30 % of the eigenfrequencies within 1 % from the exact solution. It should be noted that both the VUKIMS and the C^0/G^1SC models contain the exact same basis functions. The slight difference in number of DOFs is due to more control variables being eliminated in the C^0/G^1SC case. This elimination of variables is also the reason why the VUKIMS model happens to end up with the same number of DOFs as the single patch mesh in this case.

The larger errors in fig. 3b are partly due to the introduction of mode switching toward higher modes. This means that the modes might occur at the wrong frequency, although the mode shapes themselves might still be accurate. It is therefore worth investigating the mode shapes in more detail. Figure 4 shows convergence curves for the first non-constant eigenmode $u_{01}(x, y)$. The L^2 relative error $\|\hat{u}_{01} - u_{01,\mathrm{ex}}\|_2 / \|u_{01,\mathrm{ex}}\|_2$ is used as error criterion, with the L^2 norm defined as $\|\bullet\|_2 = \sqrt{\int_\Omega \bullet^2 \mathrm{d}\Omega}$. The VUKIMS model is about

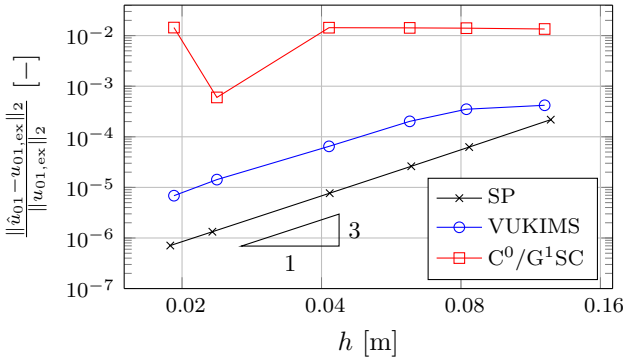

Figure 4: Convergence of the L^2 error norm for the first non-constant eigenmode versus the average element size, calculated for the different models using quadratic B-spline basis functions. Both the single patch and the VUKIMS model converge at the optimal rate.

an order of magnitude less accurate than the single patch model, but both converge with the optimal rate. However, there is no convergence when using the C^0/G^1SC method. For this relatively simple mode shape (cf. fig. 5a), the C^0/G^1SC approximation is still within an engineering accuracy of 1 %, but it quickly deteriorates with increasing mode number. Figure 5 illustrates this for a number of mode shapes, using the same 3000-DOF model as in fig. 3b. While the single patch and the VUKIMS model do not show any visual deviations from the exact solution for the presented mode shapes, the C^0/G^1SC model already shows distortions for the fourth mode. Especially for the higher modes, the accuracy strongly deteriorates around the interfaces even though the correct mode shapes are still inherently present (as can be seen by counting the number of half wavelengths present in each direction). This illustrates the danger of overconstraining the model when directly enforcing eq. (12).

To demonstrate the importance of the choice of the less refined patch as the master, a series of strongly non-conforming four-patch meshes is used — with a large difference in the number of elements across interfaces. This allows to assess the robustness of the coupling approach. Figure 6 shows the most coarse and the most refined configurations of these strongly non-conforming meshes. The coupling method using the opposite master-

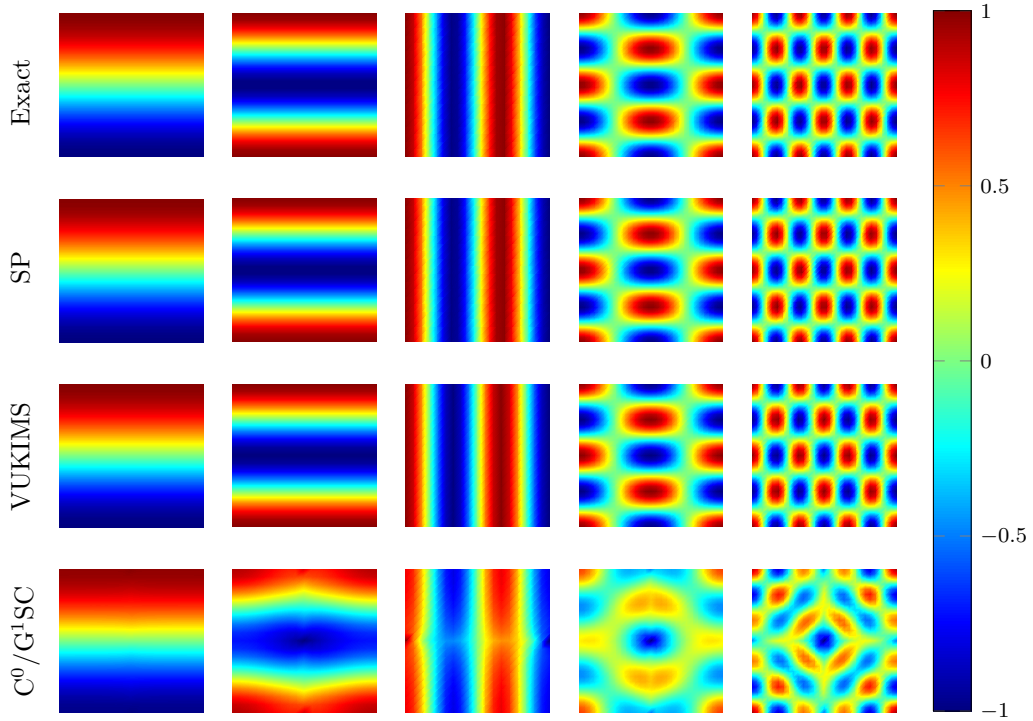

(a) 1st mode $u_{01}(x, y)$ (b) 4th mode $u_{02}(x, y)$ (c) 10th mode $u_{30}(x, y)$ (d) 20th mode $u_{24}(x, y)$ (e) 50th mode $u_{64}(x, y)$

Figure 5: Analytical mode shapes (in [Pa], considering an acoustic problem), as described by eq. (27), compared to the corresponding numerically calculated modes with the single patch (cf. fig. 2a) and with the four-patch model (cf. fig. 2b), all calculated with around 3000 DOFs as in fig. 3b). The VUKIMS approach consistently yields accurate mode shapes, even toward higher mode numbers.

slave formulation as in VUKIMS is called 'VUKISM': eq. (13) is still used, but instead of using the more refined patch as the slave (as in VUKIMS) it is used as the master. This VUKISM approach yields less interface constraints, resulting in a larger system matrix. But more importantly, it restricts the freedom on the interface to connect the non-matching basis functions; indeed, a smaller number of dependent DOFs must now be used to match the behaviour of a larger number of independent DOFs. This also means that an exact continuity enforcement for hierarchical patches is not guaranteed when using a VUKISM formulation. The VUKIMS and VUKISM approaches yield similar results as long as the non-conformity is not too severe, but the VUKISM performance starts deteriorating more rapidly as the non-conformity is more pronounced. Figure 7 shows the convergence of the first non-zero eigenfrequency and the corresponding mode shape for the strongly non-conforming models. As a reference, also the uniformly meshed single patch convergence is shown. Both the VUKIMS and the VUKISM models converge, although the VUKIMS ones do so faster. The eigenfrequency is up to three orders of magnitude more accurate with the VUKIMS coupling than with the VUKISM. The L^2 eigenmode error presents similar results, though the difference is somewhat smaller.

This eigenvalue problem demonstrates the intrinsic approximation potential of the different models. The proposed coupling method is found to yield accurate solutions,

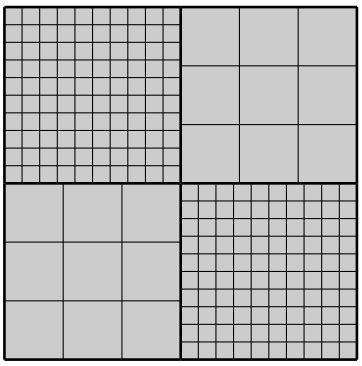

(a) Most coarse strongly non-conforming mesh, containing 218 elements.

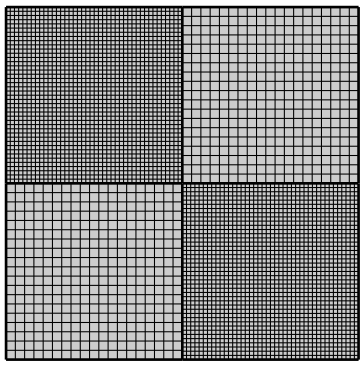

(b) Finest strongly non-conforming mesh, containing 4250 elements.

Figure 6: Topology of the strongly non-conforming meshes used for assessing the robustness of the coupling methods. The mesh in (a) is the most coarse configuration that is used, the one in (b) the most fine one. The thicker lines are the patch boundaries.

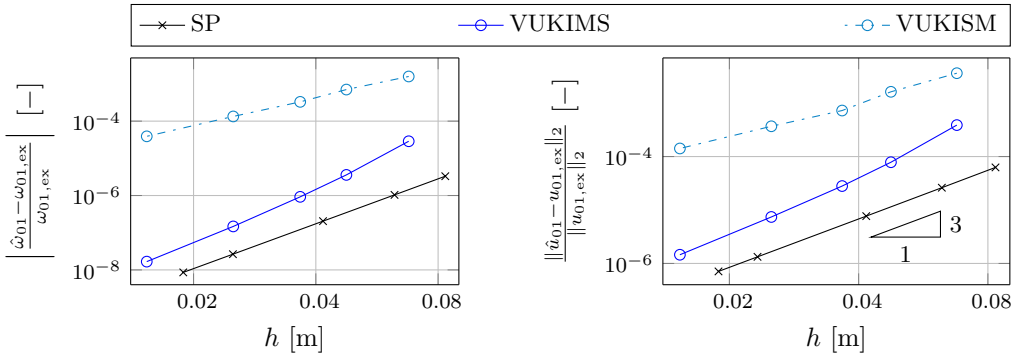

(a) Convergence of the first non-zero eigenfrequency versus the average element size. The VUKIMS coupling is two to three orders of magnitude more accurate than the VUKISM approach.

(b) Convergence of the L^2 error norm for the first non-constant eigenmode versus the average element size. This shows the same trend as the corresponding eigenfrequency convergence in (a).

Figure 7: Assessment of the accuracy of (a) the first non-zero eigenfrequency and (b) the corresponding mode shape of the unit square, calculated using strongly non-conforming meshes (cf. fig. 6).

with the four-patch VUKIMS model behaving very similarly to the single patch model. To confirm these findings for a more general setting, the next two sections study the proposed VUKIMS coupling technique in boundary value problems of more complex geometries in a C^0-continuity context.

4.1.2. Bat-shaped acoustic cavity

This section studies an internal acoustic problem in a two-dimensional bat-shaped cavity, as shown in fig. 8a. The cavity is filled with air, characterised by its speed of sound

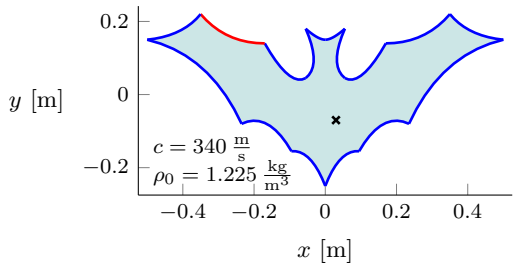

(a) Bat-shaped acoustic cavity with all boundaries rigid (in blue) except for the vibrating panel (in red) at the top of the bat's left wing. The black × marks the FRF response point.

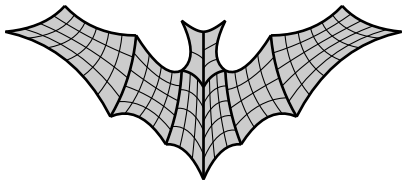

(b) Non-conforming base mesh, built using 274 quadratic B-spline DOFs and 8 patches. The thicker lines are the patch boundaries.

Figure 8: Bat-shaped acoustic cavity filled with air and excited by a unit normal velocity vibration at the top of the left wing: (a) the problem definition and (b) the employed non-conforming base mesh.

$c = 340\,\mathrm{m/s}$ and its fluid mass density $\rho_0 = 1.225\,\mathrm{kg/m^3}$. The steady-state dynamic behaviour in this acoustic domain V is described by the scalar acoustic pressure field $p_a(\boldsymbol{r})$, which is in this case governed by the homogeneous Helmholtz equation [37]:

$$\boldsymbol{\nabla}^2 p_a(\boldsymbol{r}) + k^2 p_a(\boldsymbol{r}) = 0 \qquad \boldsymbol{r} \in V, \tag{28}$$

where $\boldsymbol{r} = (x, y)$ is the position vector and $k = \frac{\omega}{c}$ the acoustic wavenumber (with ω the angular frequency). Often the frequency $f = \frac{\omega}{2\pi} = \frac{kc}{2\pi}$ or the acoustic wavelength $\lambda = \frac{2\pi}{k} = \frac{c}{f}$ is used instead of the wavenumber k or angular frequency ω. All boundaries have Neumann conditions in this case, with an imposed normal velocity $\bar{v}_n$:

$$\frac{\mathrm{j}}{\rho_0 \omega} \frac{\partial p_a(\boldsymbol{r})}{\partial n} = \bar{v}_n(\boldsymbol{r}) \qquad \boldsymbol{r} \in \Omega = \partial V. \tag{29}$$

All boundary parts are rigid ($\bar{v}_n = 0\,\mathrm{m/s}$) in this case, except for one segment at the top of the left wing (in red in the figure). That boundary segment excites the cavity with a unit normal velocity vibration ($\bar{v}_n = 1\,\mathrm{m/s}$). The cavity is modelled using eight quadratic B-spline patches, as shown in fig. 8b. Since the Helmholtz equation (28) is a second-order partial differential equation, at least C^0-continuity is needed to satisfy shape function compatibility requirements.

The acoustic pressure response $p_a(\boldsymbol{r})$ is analysed at three frequencies: 10, 500 and 2500 Hz. This allows analysing responses of varying degree of dynamic behaviour, ranging from less than a full wavelength fitting inside the problem domain to multiple wavelengths fitting within. Reference solutions are computed using a conforming mesh of more than 330000 quartic DOFs, coupling the same patches through a trivial one-to-one matching of the interface variables. Figure 9 shows these reference acoustic pressure fields. To assess the solution accuracy with respect to this reference, the following relative error ϵ_{avg} is defined:

$$\epsilon_{\mathrm{avg}}(p_a) = \frac{1}{n_p} \sum_{i=1}^{n_p} \left| \frac{p_a(\boldsymbol{r}_i) - p_{a,\mathrm{ref}}(\boldsymbol{r}_i)}{p_{a,\mathrm{ref}}(\boldsymbol{r}_i)} \right|, \tag{30}$$

with $n_p = 200$ evaluation points, spaced uniformly throughout the cavity. A series of non-conforming meshes is generated by refining the base mesh shown in fig. 8b. Again

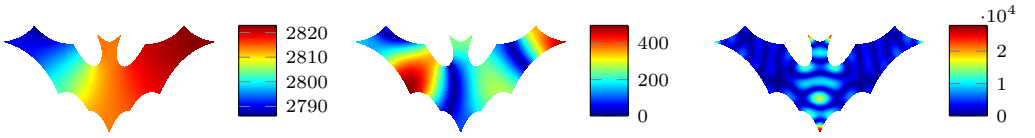

(a) 10 Hz. (b) 500 Hz. (c) 2500 Hz.

Figure 9: Reference solutions for the acoustic pressure amplitude [Pa] in the bat-shaped cavity at (a) 10 Hz, (b) 500 Hz and (c) 2500 Hz.

the original difference in the number of elements across interfaces is maintained between different refinement steps (as opposed to the original ratio of these numbers). Several patch coupling methods are tested; they are denoted and defined as follows:

VUKIMS
: The proposed VUKIMS coupling method, as explained in section 3.

C^0/G^1SC
: The C^0/G^1 method [14], using static condensation to enforce the interface constraints.

C^0/G^1PF10^X
: The C^0/G^1 method [14], using a penalty formulation to incorporate the interface constraints, with a penalty factor $a_{\text{pen}} = 10^X$ (with $X = 3, 6, 9$). This penalty formulation takes the interface constraints into account by adding a penalty matrix $\mathsf{K}_{\text{pen}} = a_{\text{pen}}\mathsf{R}^T\mathsf{R}$ to the original dynamic stiffness matrix K before solving the system, where the matrix R represents the coupling equations from eq. (12) but also contains empty entries for the non-interface DOFs $\mathbf{u}_O$.

These methods are benchmarked against solutions obtained with the same patch configuration but with a conforming mesh, using a trivial one-to-one matching of the interface variables.

Figure 10 shows convergence curves obtained with quadratic and cubic non-conforming meshes for the studied frequencies. The curves indicate the relative error ϵ_{avg} versus the total number of independent DOFs (i.e. after condensation of the dependent DOFs). They present several observations:

- Although not all curves converge, at the lowest frequency all models yield solutions within an engineering accuracy of 1 %. This is not the case for the highest frequency: in the quadratic case, only the VUKIMS and the C^0/G^1PF10^6 models become accurate once they start to converge. In the cubic case, also the C^0/G^1PF10^6 method exhibits the beginning of convergence, whereas the C^0/G^1PF10^3 variant stagnates at a 1 % error. The middle frequency results lie somewhere between.

- The VUKIMS coupling always yields good results. It performs equally well as the benchmark model with a conforming mesh.

- The C^0/G^1SC method does not converge. The penalty formulation seems to yield better results, although it is far from robust. The best choice for the penalty factor depends both on frequency and on polynomial order. A penalty factor of 10^3 appears to give the best overall results, but it also seems to consistently stagnate and is sometimes overtaken by the C^0/G^1PF10^6 variant.

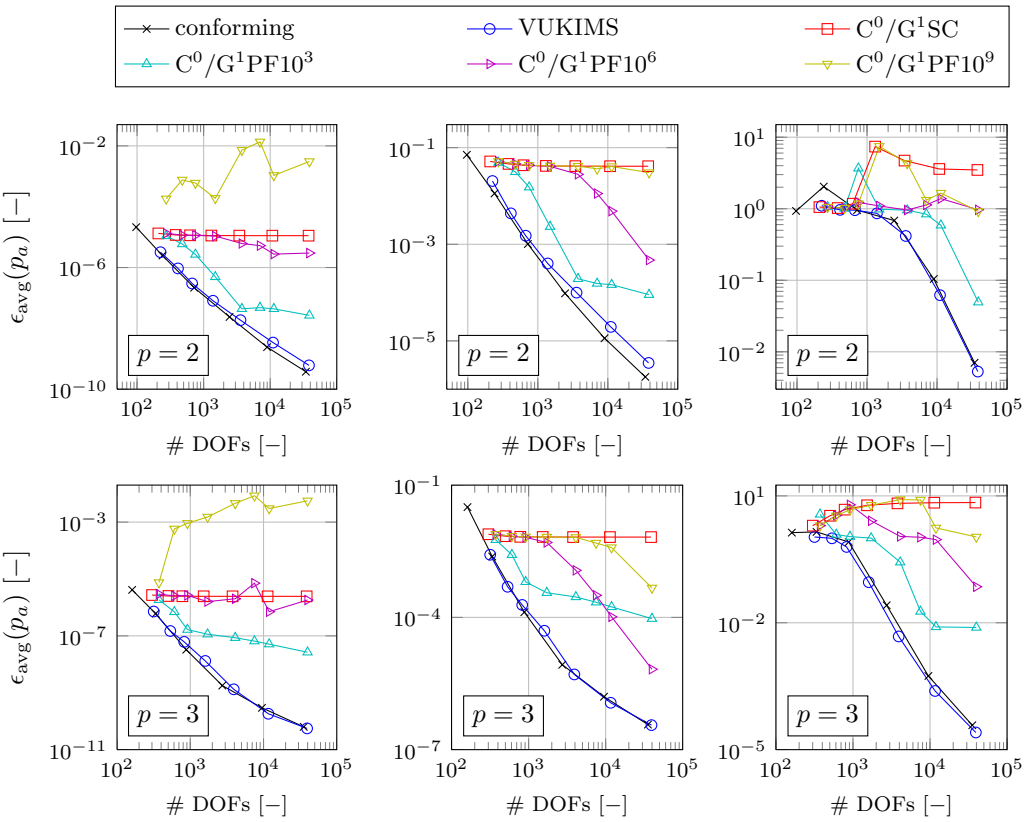

(a) 10 Hz. (b) 500 Hz. (c) 2500 Hz.

Figure 10: Convergence of the acoustic pressure in the bat-shaped cavity versus the number of independent DOFs (according to the error criterion in eq. (30)), for quadratic and cubic shape functions. The curves are calculated at various frequencies and using different coupling techniques for non-conforming meshes (fig. 8b). The proposed VUKIMS coupling performs almost equally well as a conforming mesh.

- The C^0/G^1PF10^9 curves seem to largely follow the C^0/G^1SC ones. This is understandable: a higher penalty factor enforces the interface constraints more strongly, while the C^0/G^1SC model explicitly enforces them through a static condensation method. For the lowest frequency the C^0/G^1PF10^9 models produce far worse results than the C^0/G^1SC variants, due to the interface constraints being too strongly penalised.

- As expected, the cubic models are more accurate and converge faster than the quadratic ones.

This again highlights the danger of overconstraining the interface when directly enforcing eq. (12) instead of eq. (13), which becomes more of a problem as the frequency increases.

To study the frequency behaviour in more detail, fig. 11 plots Frequency Response Function (FRF) curves showing the acoustic pressure amplitude in the point (0.03, -0.07) m (marked by a black × in fig. 8a) between 10 and 2500 Hz. The FRF is calculated with both the VUKIMS and the C^0/G^1 approach, each time with a non-conforming

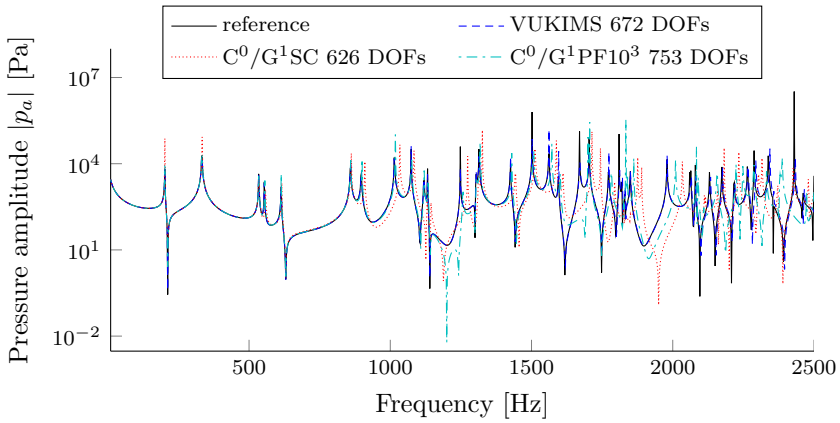

(a) 10 – 2500 Hz.

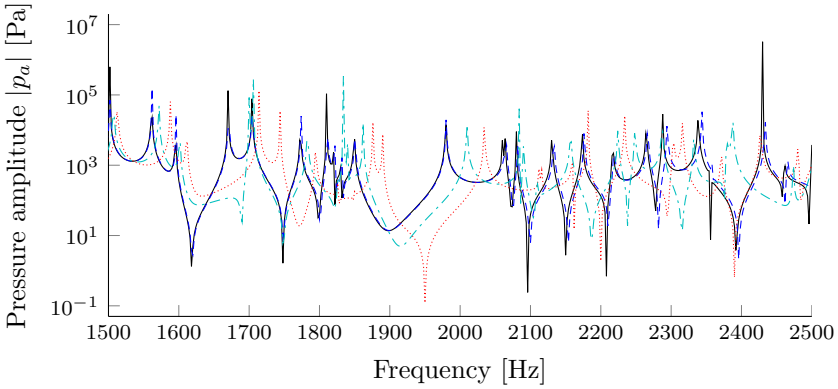

(b) Zoom of (a) between 1500 and 2500 Hz.

Figure 11: FRF curves showing the frequency-dependent acoustic pressure amplitude in the point located at (0.03, -0.07) m, calculated with different non-conforming patch coupling methods. The reference model is a fourth-order conforming mesh of more than 85000 DOFs. All the other curves are calculated with the same non-conforming mesh of 477 quadratic elements, using a frequency resolution of 2 Hz.

quadratic mesh containing 477 elements. For the C^0/G^1 coupling, both the static condensation variant and the penalty formulation with a penalty factor of 10^3 are calculated. After taking into account the interface constraints, the VUKIMS model contains 626 independent DOFs, and the C^0/G^1SC and the C^0/G^1PF10^3 respectively 672 and 753 DOFs. These models are compared to a reference FRF, computed with a conforming mesh of more than 85000 quartic DOFs. As fig. 11a shows, all models follow the reference quite well up to about 800 Hz. Increasing the frequency further introduces a frequency shift of the C^0/G^1SC response with respect to the reference. This is a well-known phenomenon called the dispersion effect, which leads to unwanted pollution errors [38–40]. The VUKIMS and the $C^0/G^1 10^3$ models do not experience a frequency shift below 1500 Hz, but the $C^0/G^1 10^3$ accuracy is not very consistent and does not always exhibit the correct frequency behaviour. It shows for instance a fictitious anti-resonance

around 1200 Hz. When increasing the frequency even further, the accuracy of all the non-conforming models decreases. Figure 11b zooms in on the frequency region between 1500 and 2500 Hz. The VUKIMS coupling continues to follow the reference very well up to about 2100 Hz, where it also starts to show a frequency shift — but still exhibits the same dynamic behaviour.

4.1.3. Strongly non-conforming multipatch sphere scattering an acoustic plane wave

This section presents a three-dimensional acoustic problem, illustrating a C^0-coupling of three-dimensional NURBS surface patches. Consider a rigid sphere of radius R suspended in an unbounded acoustic medium. If a plane pressure wave of unit amplitude and wavenumber k impinges on this sphere, the resulting scattered acoustic pressure field $p_s(r,\theta)$ can be calculated analytically as an infinite sum [41]:

$$p_s(r,\theta) = \sum_{\nu=0}^{\infty} -(2\nu+1)\mathrm{j}^\nu \frac{(\nu+1)j_{\nu+1}(kR) - \nu j_{\nu-1}(kR)}{(\nu+1)h^{(2)}_{\nu+1}(kR) - \nu h^{(2)}_{\nu-1}(kR)} P_\nu(-\cos\theta) h^{(2)}_\nu(kr), \tag{31}$$

with r the radial distance from the sphere's centre and θ the accompanying azimuthal angle (measured with respect to the plane wave propagation direction). The function P_ν is the Legendre polynomial, j_ν the spherical Bessel function of the first kind, and $h^{(2)}_\nu$ the spherical Hankel function of the second kind, all of order ν.

The acoustic pressure in this problem setting is governed by the Helmholtz equation (28), but due to the unbounded character of the domain, a boundary element formulation is more suited for numerically solving it. Such a formulation relates the acoustic pressure in the problem domain to the distribution of potential functions on the boundary surface, inherently taking into account non-reflecting boundary conditions towards infinity. This section presents the performance of a strongly non-conforming multipatch mesh when used for solving this scattering problem in an isogeometric variational boundary element framework [34], which requires C^0-continuity.

The study is carried out at a frequency of 100 Hz with the following problem parameters: $R = 1\,\mathrm{m}$, $c = 340\,\mathrm{m/s}$ and $\rho_0 = 1.225\,\mathrm{kg/m^3}$. Since the sphere is rigid, a velocity boundary condition (29) with $\bar{v}_n = 0\,\mathrm{m/s}$ is imposed. Figure 12 plots the analytical scattered pressure field at the sphere's surface. Due to the nature of the problem, this field is rotationally symmetric around the plane wave's propagation vector passing through the sphere's centre. Figure 13a shows the non-conforming NURBS surface mesh that

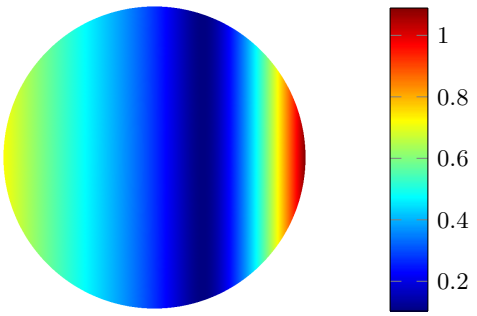

Figure 12: Colour plot of the analytical scattered pressure field [Pa] on the sphere's surface, with respect to the analytical solution from eq. (31). The impinging plane wave is travelling from left to right.

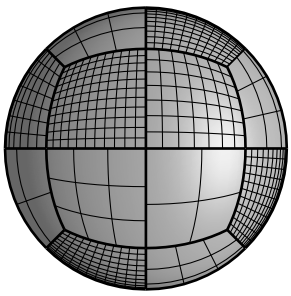

(a) Side view of the non-conforming mesh of a sphere, consisting of 24 identically sized bi-quartic NURBS surface patches, which results in 2586 uncoupled DOFs. Thick lines indicate the patch boundaries. The non-visible side of the mesh contains the same non-conformities.

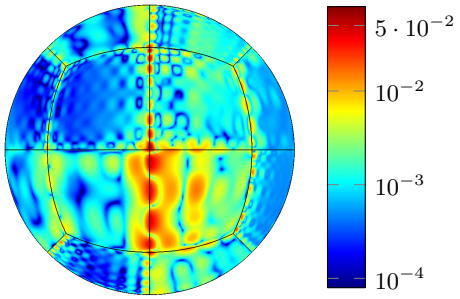

(b) Corresponding relative error [–] of the scattered acoustic pressure at the sphere's surface, with respect to the analytical solution of eq. (31) (cf. fig. 12). The impinging plane wave is travelling from left to right.

Figure 13: Calculation of the scattered acoustic pressure with a strongly non-conforming multi-patch mesh.

is used for modelling the sphere's boundary. It consists of 24 quartic NURBS patches and contains 2586 DOFs before coupling, which results in 2008 DOFs after the VUKIMS coupling. Figure 13b shows the corresponding relative error with respect to the analytical reference solution from eq. (31). As expected, the more coarse patches clearly perform worse than the more refined ones. But the overall accuracy is good, with an average relative error value of 0.19 %. Due to the non-conformities, the error values are larger at the patch interfaces. Nonetheless, the error plot shows the good coupling between the 24 patches — the relative error does not exceed 8.3 % anywhere. It should be noted that along the strongly non-conforming interfaces, the solution is in fact more accurate than along the weaker non-conformities. This illustrates that the coupling method is inherently the least accurate when the bordering patches are non-conforming but have a nearly equal number of elements. Indeed, such configurations have the lowest degree of flexibility to ensure the correct continuity enforcement between the bordering but non-matching discretisations. If the non-conformities are more pronounced (i.e. the numbers of elements differ more), the finer mesh in the slave patch introduces extra DOFs that facilitate the coupling.

For comparison purposes, fig. 14 shows the performance of the same patch configuration as in fig. 13a but this time using a conforming discretisation. The coupling across patches is then done by a trivial one-to-one matching of the corresponding interface DOFs. Due to the more uniform element size, the relative error is more uniformly distributed (not exceeding 1.1 % anywhere) and on average slightly lower: 0.13 %.

4.2. C^1-coupling: Kirchhoff-Love shell structures

The current section presents two examples of a C^1-coupling for Kirchhoff-Love shell structures to illustrate that the proposed coupling method can also accurately enforce higher-order continuities.

4.2.1. Dynamic bending of a rectangular plate

The dynamic Kirchhoff-Love plate problem is first briefly introduced, and then a rectangular multipatch example problem is presented to further validate and benchmark the

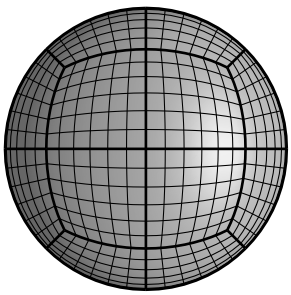

(a) The same patch configuration as shown in fig. 13a, but using a conforming discretisation. This model contains 2400 quartic NURBS basis functions, which results in 1946 independent DOFs.

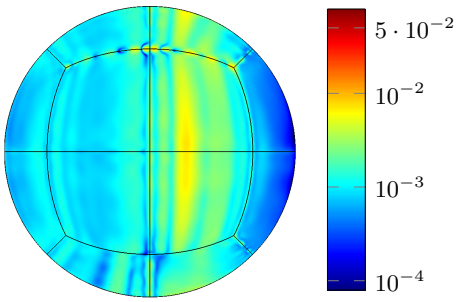

(b) Corresponding relative error [–] of the scattered acoustic pressure at the sphere's surface, with respect to the analytical solution of eq. (31) (cf. fig. 12). The impinging plane wave is travelling from left to right.

Figure 14: Calculation of the scattered acoustic pressure with a conforming multipatch mesh.

VUKIMS coupling method. In particular also a strongly non-conforming patch configuration is treated to demonstrate the method's robustness.

Consider a thin, flat plate of thickness t, and of a homogeneous, isotropic and linearly elastic material of density ρ_s, Young's modulus E and Poisson's coefficient ν. The plate lies in the xy-plane and is excited by an external load that is applied in the direction normal to the plate surface (the z-direction), i.e. there is no in-plane loading, only bending. The Kirchhoff-Love plate theory makes the kinematic assumption that a straight line normal to the plate's mid-surface is inextensible and remains straight and normal to the mid-surface after deformation [42]. This means that the deformed plate does not undergo any transverse shear deformation, and that there is no stress normal to the plate surface. The transverse displacement $w(x, y)$ of the plate's mid-surface ($z = 0$) fully describes the out-of-plane bending motion. Assuming a harmonic time-dependency, the steady-state dynamic equation of bending motion $w(x, y)$ in a thin flat plate is then governed by the following equation [43]:

$$\boldsymbol{\nabla}^4 w(\boldsymbol{r}) - k_b^4 \cdot w(\boldsymbol{r}) = \frac{p(\boldsymbol{r})}{D}, \tag{32}$$

with $\boldsymbol{r} = (x, y)$, where $\boldsymbol{\nabla}^4 \bullet = \frac{\partial^4 \bullet}{\partial x^4} + \frac{\partial^4 \bullet}{\partial x^2 \partial y^2} + \frac{\partial^4 \bullet}{\partial y^4}$ is the biharmonic operator and $p(x, y)$ the external (normal) load. The bending stiffness D and the bending wavenumber k_b are defined as:

$$D = \frac{Et^3}{12(1-\nu^2)}, \tag{33}$$

$$k_b = \sqrt[4]{\frac{\rho_s t \omega^2}{D}}, \tag{34}$$

where ω is again the angular frequency (cf. section 4.1.2). Since eq. (32) is a fourth-order partial differential equation, the shape function compatibility requires at least C^1-continuity. A rotationless formulation is used here, with only the transverse displacement as degree of freedom (and no rotations). The collinearity of the control variables is used to enforce the rotational continuity, as explained in section 3.3.

Figure 15a sketches the plate bending problem that is studied in this work. It concerns a rectangular steel plate ($\rho_s = 7800\,\mathrm{kg/m^3}$, $E = 200\,\mathrm{GPa}$, $\nu = 0.3$) of dimensions 1 m

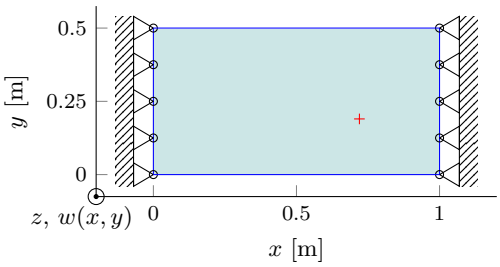

(a) Top view of the rectangular plate, simply supported at the left and right edges. The red + marks the force application point.

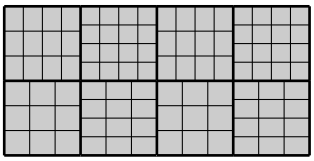

(b) Non-conforming base mesh, built using 8 B-spline patches. The thicker lines are the patch boundaries.

Figure 15: Rectangular steel plate of dimensions 1 m × 0.5 m and with a thickness of 5 mm: (a) the problem sketch and (b) the employed non-conforming base mesh.

× 0.5 m and with a thickness $t = 5$ mm. The left and right edges are simply supported, imposing a zero displacement and zero normal bending moment. The top and bottom edge are free edges, not constraining the displacements in any way. A point force of 1 kN excites the plate at the point (0.72, 0.19) m (marked by the red + in fig. 15a). The problem is studied at three frequencies: 100, 500 and 1500 Hz. Reference solutions $w_{\text{ref}}(x, y)$ for the transverse displacements are computed using a single patch mesh of more than 20000 quintic DOFs. Figure 16 shows these reference transverse displacements. The problem is analysed using a series of non-conforming meshes, starting from the one shown in fig. 15b. Again, the original difference in the number of elements across interfaces is maintained between different refinement steps (as opposed to the original ratio of these numbers). Both the proposed VUKIMS and the C^0/G^1 methods C^0/G^1SC and C^0/G^1PF10^X are again compared, but now they are also benchmarked against solutions obtained with a uniformly meshed single patch model. Figure 17 plots convergence curves for shape functions of various polynomial orders at the three different frequencies, using the following error criterion:

$$\epsilon_{\text{avg}}(w) = \frac{1}{n_p} \sum_{i=1}^{n_p} \left| \frac{w(x_i, y_i) - w_{\text{ref}}(x_i, y_i)}{w_{\text{ref}}(x_i, y_i)} \right|, \tag{35}$$

with again $n_p = 200$ evaluation points (spaced uniformly throughout the plate).

The accuracy generally decreases with increasing frequency and with decreasing polynomial order, as expected. At 1500 Hz the quadratic models require a very fine mesh in order to yield a reasonable error, which is why cubic and quartic results are shown. The VUKIMS coupling again matches the performance of the single patch model very well. In

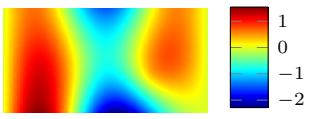

(a) 100 Hz.

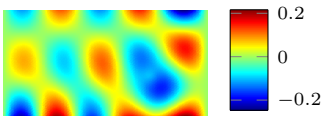

(b) 500 Hz.

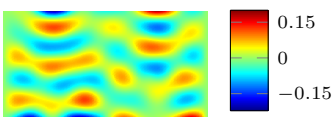

(c) 1500 Hz.

Figure 16: Reference solutions for the harmonic transverse displacement [mm] of the simply supported rectangular plate at different frequencies.

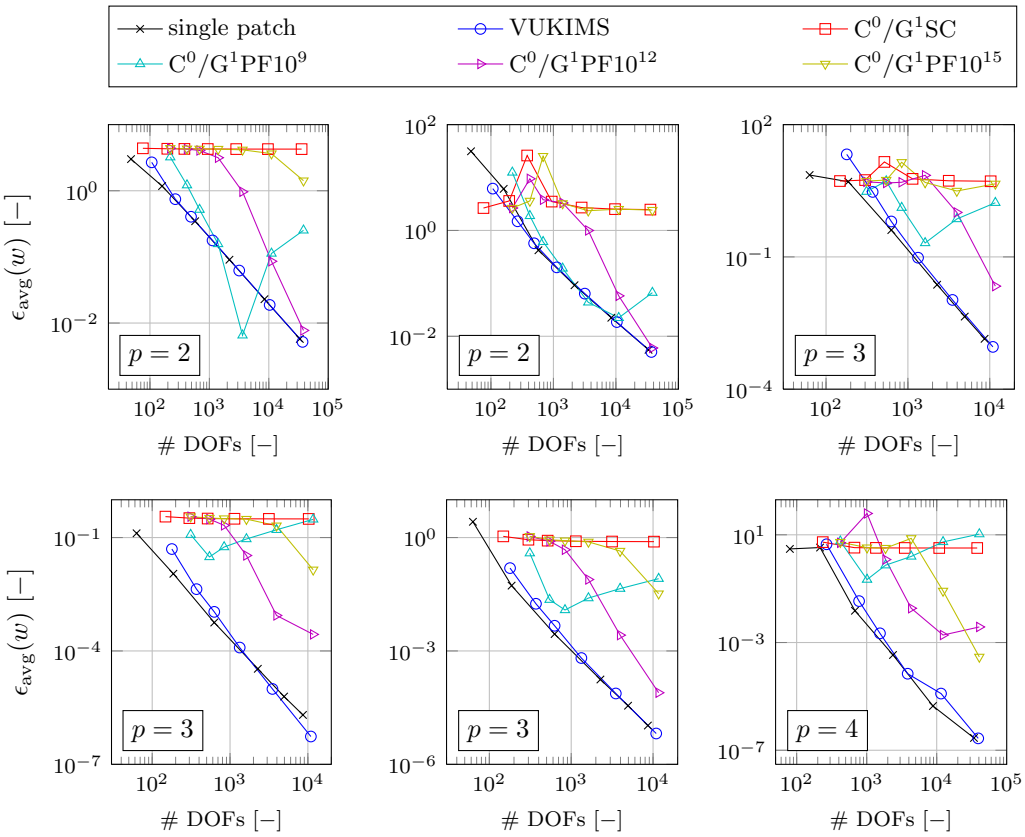

(a) 100 Hz. (b) 500 Hz. (c) 1500 Hz.

Figure 17: Convergence of the transverse displacement in the rectangular plate versus the number of independent DOFs (according to the error criterion in eq. (30)), for different polynomial orders p. The curves are calculated at various frequencies and using different coupling techniques for non-conforming meshes (fig. 15b). A single patch mesh of over 20000 quintic DOFs is used a reference model. The proposed VUKIMS coupling matches the performance of the single patch models.

comparison to the acoustic problem, higher penalty coefficients have to be used here for the C^0/G^1PF method to obtain reasonable results. Overall, a penalty factor of 10^9 seems to perform best for the quadratic models (although not very consistently), but in the cubic case the C^0/G^1PF10^{12} performs better. In general, the C^0/G^1PF models seem to not converge monotonically, and the static condensation variant does not yield accurate results at any frequency.

It is also interesting to study the accuracy of the different coupling methods on the interfaces themselves. For that purpose, a strongly non-conforming mesh is used, as shown in fig. 18. This mesh consists of 2450 elements, of which the most coarse patches contain 64 elements each (8×8), and the finest ones 729 each (27×27). Quadratic B-spline basis functions are used, resulting in 3042 (uncoupled) DOFs. This leads to 2400, 2764, 2260 and 2964 DOFs for the VUKIMS, VUKISM, C^0/G^1SC and C^0/G^1PF methods, respectively (after coupling and enforcement of boundary conditions). Figure 19 shows the solutions of these different models at 500 Hz. Apart from the C^0/G^1SC approach, all

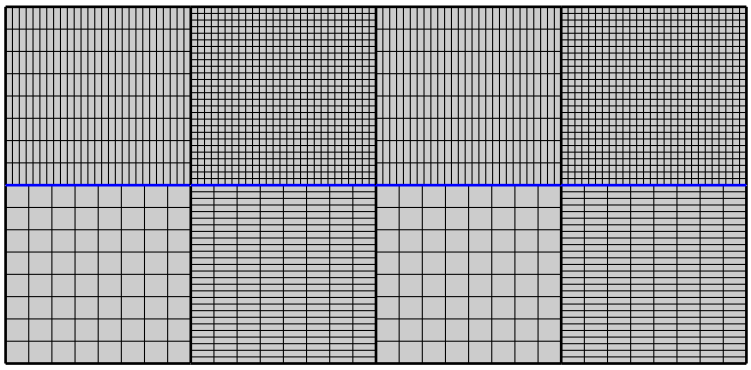

Figure 18: Strongly non-conforming mesh of the rectangular plate, consisting of 2450 elements. The thicker lines are the patch boundaries. The blue line is the collection of interfaces analysed here.

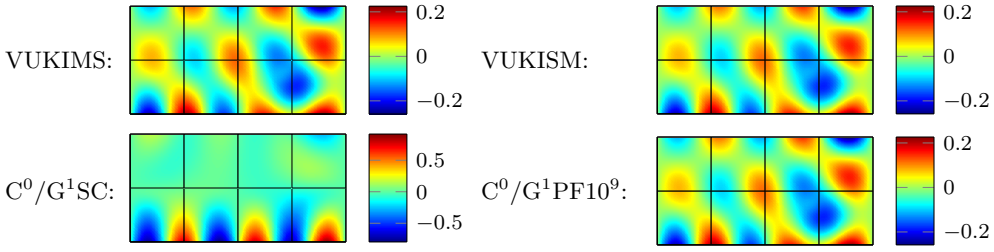

Figure 19: Contour plots of the harmonic transverse displacement [mm] at 500 Hz calculated with the mesh from fig. 18 using different coupling methods. Patch boundaries are indicated in black. All the plots visually match the reference solution (fig. 16b) except for the C^0/G^1SC model.

the models seem to match the reference model well. These solutions are now studied in more detail along the interface marked in blue (at $y = 0.25\,\mathrm{m}$). Figure 20 shows both the transverse displacement and its normal derivative (with respect to the interface) along this line for the different methods. Curves are shown that evaluate the solution using data from the patches on either side of the interface. Also the reference solution (the same as used above) is plotted. Although the VUKIMS and the VUKISM curves appear to be very similar, the zoomed plot insets in fig. 20b show that in the VUKISM case there are small oscillations visible in the normal derivative corresponding to the finer patches. These do not show up in the VUKIMS model. The insets also show that the proposed VUKIMS coupling maintains a better C^1-continuity than the C^0/G^1PF10^9 model, with a slightly better match between the patches. This can be seen more clearly in fig. 21, that plots the (absolute) errors in C^0- and C^1-continuity along the interface according to the following error criteria:

$$\Delta C^0_{\mathrm{int}}(x) = \left| w(x)\big|_{\mathrm{int}+} - w(x)\big|_{\mathrm{int}-} \right| \qquad \Delta C^1_{\mathrm{int}}(x) = \left| \frac{\partial w}{\partial y}(x)\Big|_{\mathrm{int}+} - \frac{\partial w}{\partial y}(x)\Big|_{\mathrm{int}-} \right|, \tag{36}$$

where $\bullet\big|_{\mathrm{int}+}$ and $\bullet\big|_{\mathrm{int}-}$ refer to the multipatch model quantities evaluated using the variables belonging to either side of the interface. It is important to note that these error

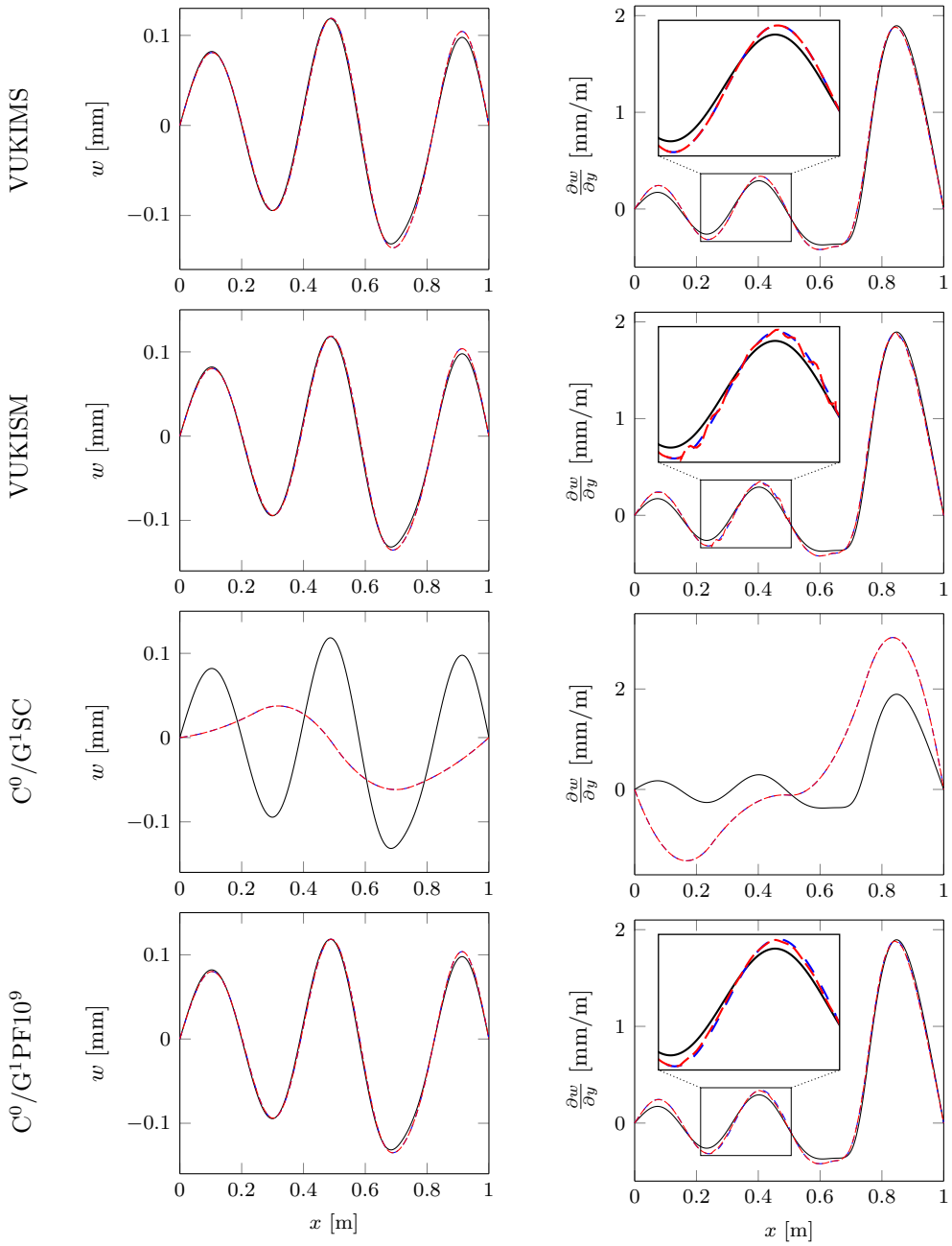

(a) Transverse displacement along the interface line.

(b) Slope of the transverse displacement normal to the interface.

Figure 20: Assessment of the solution accuracy on the blue interface line of fig. 18 at 500 Hz (cf. fig. 19), comparing data from the patches below the interface (- - -) and above it (- - - -) to the reference solution (——).

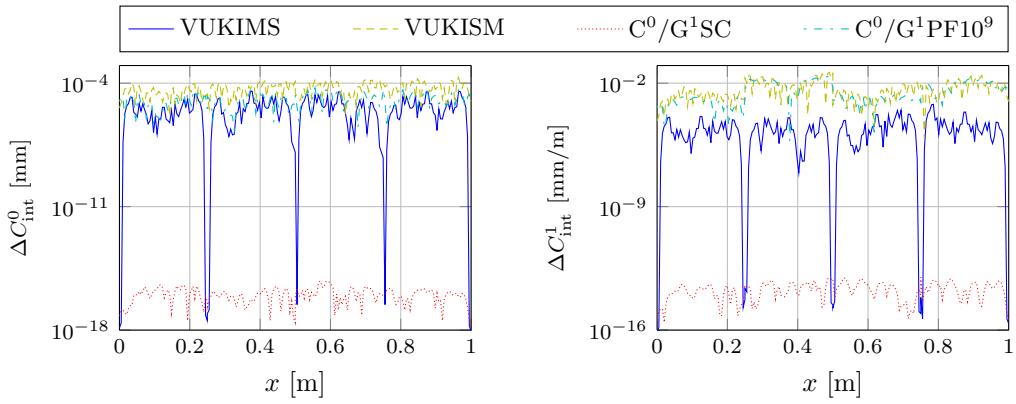

(a) Error for the C^0-continuity.

(b) Error for the C^1-continuity.

Figure 21: Absolute errors in (a) C^0- and (b) C^1-continuity along the blue interface line ($y = 0.25\,\text{m}$) in fig. 18 for the different coupling methods (cf. fig. 20), according to eq. (36). Of the models that yield accurate solutions, the proposed VUKIMS coupling results in the best continuity enforcement.

criteria are not at all measures of the solution accuracy, but simply of the extent to which the continuity requirements are satisfied. The curves in fig. 21 indicate that the C^0/G^1SC method results in an exact continuity enforcement, with continuity errors in the order of the machine precision. Of the methods that yield accurate solutions, the proposed VUKIMS technique leads to the best continuity enforcement — especially regarding C^1-continuity. The continuity errors for the C^0/G^1PF model could possibly be decreased by manually finetuning the penalty factor further. Also note the error values near machine precision at the patch edges ($x = 0.25\,,\,0.5\,,\,0.75\,\text{m}$) for the VUKIMS coupling; this is the result of the locally interpolatory character of the basis functions and the method's one-to-one matching of the control variables at patch intersection points. This is not the case for the VUKISM or the C^0/G^1PF method, which both have to relax on the one-to-one matching of these intersection DOFs to accommodate the (higher number of) remaining interface constraints.

4.2.2. Scordelis-Lo roof benchmark

This section studies the C^1-coupling of a curved Kirchhoff-Love shell structure, where bending and membrane deformation interact with each other. These isogeometric shells are again rotationless, resulting in three translational DOFs per control point. In particular, the problem under study here is the Scordelis-Lo roof benchmark, a part of the well-known shell obstacle course proposed by Belytschko et al. [44]. It consists of a simply supported cylindrical shell section uniformly loaded by gravity, as described in fig. 22a. The benchmark value is the vertical displacement of the midpoint of the straight side edges.

The problem is studied using a single patch topology, as well as with non-conforming four-patch meshes, like the one shown in fig. 22b. This figure also shows a reference deformation plot calculated with a quintic single patch model of 10 000 elements (resulting in more than 33 000 DOFs). Figure 23 shows the performance of different kinds of models: a single patch ('SP') model, a non-conforming four-patch model ('4P-NC'), and a conforming variant of the same patch configuration ('4P C'). All models contain biquadratic

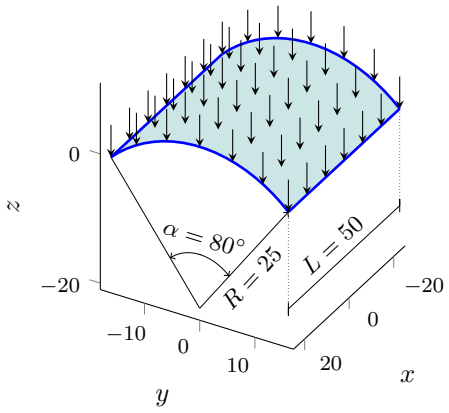

thickness t:	0.25
Young's modulus E:	$4.32 \cdot 10^8$
Poisson's ratio ν:	0
gravity loading g:	90 per unit area

(a) Problem setting, consisting of a cylindrical section loaded uniformly by gravity. The straight edges are free, while the curved edges are constrained from moving in y- and z-direction.

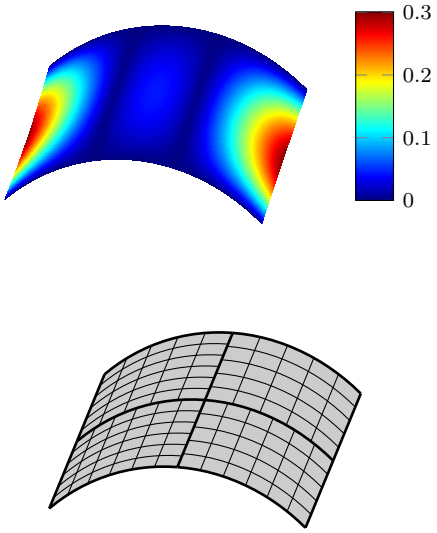

(b) *top:* Reference solution (calculated with a quintic single patch model of 10 000 elements), showing a colour plot of the vertical displacement.
bottom: The non-conforming mesh used for analysis, with the patch boundaries indicated by the thick lines.

Figure 22: The Scordelis-Lo roof benchmark description.

NURBS basis functions. Figure 23a shows the convergence to the reference solution of 0.3024 as given by [44]. Visually all models seem to approach this reference value well, although they converge to a value 0.3006. This is slightly lower than the Belytschko reference, an observation that is consistent with the work of Kiendl et al. on isogeometric Kirchhoff-Love shells [10]. If only the C^0-continuity is enforced, the solution converges to a benchmark value of 0.4074, indicating the importance of also coupling the shape function derivatives. For a more detailed error estimate for the different models, fig. 23b shows convergence curves of the relative error with respect to a single patch reference solution (cf. fig. 23). The performance of the non-conforming multipatch model is the same as that of the conforming ones, and both are nearly identical to the single patch convergence.

5. Conclusion

A weak patch coupling method is presented for satisfying continuity requirements between non-conforming NURBS patches, with its main merit being its simplicity and flexibility. The coupling relationships are derived using virtual uncommon knot insertion and a master-slave formulation. They can be computed using only the interface knot vectors and NURBS weights in an inexpensive pre-processing step. The resulting interface constraints are linear equations that can be enforced through simple matrix condensation, thereby even reducing the system matrix size. This coupling procedure is independent of any problem-specific factors; as such, it operates on a mathematical level and not on

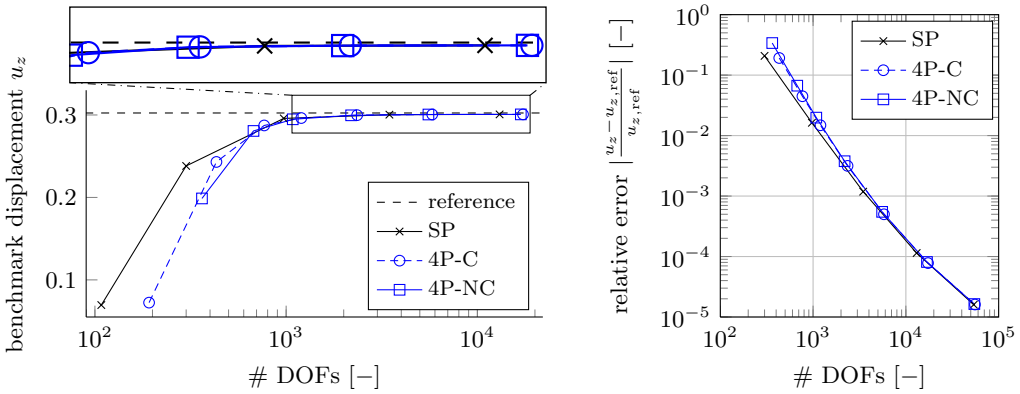

(a) Convergence to the reference solution from [44].

(b) Convergence of the relative error with respect to a single patch reference solution.

Figure 23: Convergence of the vertical displacement at the midpoint of the free edge of the Scordelis-Lo roof, calculated using different mesh topologies. The conforming four-patch models (4P-C) as well as the non-conforming ones (4P-NC) converge to the same solution as the single patch model (SP).

a physical one, making it very versatile toward problem types it can handle. Numerical examples of both C^0- and C^1-coupling of non-conforming, non-hierarchical patch configurations are investigated, studying an analytical eigenvalue problem, and time-harmonic acoustics and (dynamic) thin plate bending as boundary value problems. Benchmarking of the proposed method versus existing similar techniques illustrates its superior accuracy, in particular toward higher frequencies and on patch interfaces. The studied boundary value problems indicate that on a per-DOF basis the presented VUKIMS approach performs equally well as conforming or even single patch models. The coupling of strongly non-conforming patches in addition demonstrates its robustness with respect to arbitrary mesh non-conformities.

Acknowledgements

The research of Laurens Coox is funded by a PhD grant of the agency of Innovation by Science and Technology in Flanders (IWT Flanders). The IWT Flanders is in addition gratefully acknowledged for its support of the OPTIWIND project. The presented work is also partially supported by the Research Fund KU Leuven and by Flanders Make, the strategic research centre for the manufacturing industry.

References

[1] T. Hughes, J. Cottrell, Y. Bazilevs, Isogeometric analysis: CAD, finite elemens, NURBS, exact geometry and mesh refinement, Computer Methods in Applied Mechanics and Engineering 194 (2005) 4135–4195.

[2] J. Cottrell, T. Hughes, Y. Bazilevs, Isogeometric Analysis: Toward Integration of CAD and FEA, John Wiley & Sons, 2009.

[3] V. P. Nguyen, C. Anitescu, S. P. Bordas, T. Rabczuk, Isogeometric analysis: an overview and computer implementation aspects, Mathematics and Computers in Simulation 117 (2015) 89–116.

[4] Y. Bazilevs, V. Calo, J. Cottrell, J. Evans, T. Hughes, S. Lipton, M. Scott, T. Sederberg, Isogeometric analysis using T-splines, Computer Methods in Applied Mechanics and Engineering 199 (2010) 229–263.

[5] M. Scott, X. Li, T. Sederberg, T. Hughes, Local refinement of analysis-suitable T-splines, Computer Methods in Applied Mechanics and Engineering 213 (2012) 206–222.

[6] D. Burkhart, B. Hamann, G. Umlauf, Iso-geometric finite element analysis based on Catmull-Clark subdivision solids, Computer Graphics Forum 29 (2010) 1575–1584.

[7] X. Wei, Y. Zhang, T. Hughes, M. Scott, Truncated hierarchical CatmullClark subdivision with local refinement, Computer Methods in Applied Mechanics and Engineering 291 (2015) 1–20.

[8] J. Deng, F. Chen, X. Li, C. Hu, W. Tong, Z. Yang, Y. Feng, Polynomial splines over hierarchical T-meshes, Graphical Models 70 (2008) 76–86.

[9] J. Cottrell, T. Hughes, A. Reali, Studies of refinement and continuity in isogeometric structural analysis, Computer Methods in Applied Mechanics and Engineering 196 (2007) 4160–4183.

[10] J. Kiendl, K.-U. Bletzinger, J. Linhard, R. Wüchner, Isogeometric shell analysis with Kirchhoff-Love elements, Computer Methods in Applied Mechanics and Engineering 198 (2009) 3902–3914.

[11] J. Kiendl, Y. Bazilevs, M.-C. Hsu, R. Wüchner, K.-U. Bletzinger, The bending strip method for isogeometric analysis of Kirchhoff-Love shell structures comprised of multiple patches, Computer Methods in Applied Mechanics and Engineering 199 (2010) 2403–2416.

[12] S. Shojaee, E. Izadpanah, N. Valizadeh, J. Kiendl, Free vibration analysis of thin plates by using a NURBS-based isogeometric approach, Finite Elements in Analysis and Design 61 (2012) 23–34.

[13] R. Schmidt, R. Wüchner, K.-U. Bletzinger, Isogeometric analysis of trimmed NURBS geometries, Computer Methods in Applied Mechanics and Engineering 241–244 (2012) 93–111.

[14] Z. Lei, F. Gillot, L. Jezequel, A C^0/G^1 multiple patches connection method in isogeometric analysis, Applied Mathematical Modelling 39 (2015) 4405–4420.

[15] M. Breitenberger, A. Apostolatos, B. Philipp, R. Wüchner, K.-U. Bletzinger, Analysis in computer aided design: Nonlinear isogeometric B-Rep analysis of shell structures, Computer Methods in Applied Mechanics and Engineering 284 (2015) 401–457.

[16] W. Dornisch, G. Vitucci, S. Klinkel, The weak substitution method — an application of the mortar method for patch coupling in NURBS-based isogeometric analysis, International Journal for Numerical Methods in Engineering 103 (2015) 205–234.

[17] X. Du, G. Zhao, W. Wang, Nitsche method for isogeometric analysis of Reissner-Mindlin plate with non-conforming multi-patches, Computer Aided Geometric Design 35–36 (2015) 121–136.

[18] E. Brivadis, A. Buffa, B. Wohlmuth, L. Wunderlich, Isogeometric mortar methods, Computer Methods in Applied Mechanics and Engineering 284 (2015) 292–319.

[19] M. Ruess, D. Schillinger, A. Özcan, E. Rank, Weak coupling for isogeometric analysis of non-matching and trimmed multi-patch geometries, Computer Methods in Applied Mechanics and Engineering 269 (2014) 46–71.

[20] V. Nguyen, P. Kerfriden, M. Brino, S. Bordas, E. Bonisoli, Nitsche's method for two and three dimensional NURBS patch coupling, Computational Mechanics 53 (2014) 1163–1182.

[21] A. Apostolatos, R. Schmidt, R. Wüchner, K.-U. Bletzinger, A Nitsche-type formulation and comparison of the most common domain decomposition methods in isogeometric analysis, International Journal for Numerical Methods in Engineering 97 (2014) 473–504.

[22] S. K. Kleiss, C. Pechstein, B. Jüttler, S. Tomar, IETI – Isogeometric Tearing and Interconnecting, Computer Methods in Applied Mechanics and Engineering 247–248 (2012) 201–215.

[23] C. Hesch, P. Betsch, Isogeometric analysis and domain decomposition methods, Computer Methods in Applied Mechanics and Engineering 213–216 (2012) 104–112.

[24] F. Ben Belgacem, The Mortar finite element method with Lagrange multipliers, Journal of Numerical Mathematics 84 (1999) 173–197.

[25] C. Bernardi, Y. Maday, T. Patera, Domain Decomposition by the Mortar Element Method, Kluwer Academic Publishers, 1993, Ch. Asymptotic and Numerical Methods for Partial Differential Equations with Critical Parameters, pp. 269–286.

[26] L. Piegl, W. Tiller, The NURBS Book, Springer-Verlag Berlin Heidelberg, 1997.

[27] M. Cox, The numerical evaluation of B-splines, DNAC 4, National Physics Laboratory (1971).

[28] C. de Boor, On calculation with B-splines, Journal of Approximation Theory 6 (1972) 50–62.

[29] M. J. Borden, M. A. Scott, J. A. Evans, T. J. Hughes, Isogeometric finite element data structures based on Bézier extraction of NURBS, International Journal for Numerical Methods in Engineering 87 (2011) 15–47.

[30] P. Kagan, A. Fischer, P. Z. Bar-Yoseph, Mechanically based models: Adaptive refinement for B-spline finite element, International Journal for Numerical Methods in Engineering 57 (2003) 1145–1175.

[31] T. F. Chan, P. C. Hansen, Some applications of the rank-revealing QR factorization, SIAM Journal on Scientific Computing 13 (1992) 727–741.

[32] C. de Falco, A. Reali, R. Vázquez, GeoPDEs: a research tool for Isogeometric Analysis of PDEs, Advances in Engineering Software 42 (2011) 1020–1034.
URL http://geopdes.sourceforge.net/

[33] L. Coox, E. Deckers, D. Vandepitte, W. Desmet, A performance study of NURBS-based isogeometric analysis for interior two-dimensional time-harmonic acoustics, Computer Methods in Applied Mechanics and Engineering 305 (2016) 441–467.

[34] L. Coox, O. Atak, D. Vandepitte, W. Desmet, An isogeometric indirect boundary element method for solving acoustic problems in open-boundary domains, Computer Methods in Applied Mechanics and Engineering (2016). *In press.* doi:10.1016/j.cma.2016.05.039.

[35] R. Simpson, M. Scott, M. Taus, D. Thomas, H. Lian, Acoustic isogeometric boundary element analysis, Computer Methods in Applied Mechanics and Engineering 269 (2014) 265–290.

[36] J. W. Brown, R. V. Churchill, Fourier Series and Boundary Value Problems, McGraw-Hill, 1993.

[37] P. Morse, K. Ingard, Theoretical Acoustics, Princeton University Press, 1968.

[38] F. Ihlenburg, I. Babuška, Finite Element Solution of the Helmholtz Equation with High Wave Number Part I: The h-Version of the FEM, Computers & Mathematics with Applications 30 (1995) 9–37.

[39] F. Ihlenburg, I. Babuška, Finite Element Solution of the Helmholtz Equation with High Wave Number Part II: The h-p-Version of the FEM, SIAM Journal of Numerical Analysis 34 (1997) 315–358.

[40] P. Bouillard, F. Ihlenburg, Error estimation and adaptivity for the finite element method in acoustics: 2D and 3D applications, Computer Methods in Applied Mechanics and Engineering 176 (1999) 147–163.

[41] E. Skudrzyk, The Foundations of Acoustics – Basic Mathematics and Basic Acoustics, Springer-Verlag New York Wien, 1971.

[42] J. Reddy, Theory and Analysis of Elastic Plates and Shells, CRC Press, 2007.

[43] R. Craig, A. Kurdila, Fundamentals of Structural Dynamics, John Wiley & Sons, Inc., 2006.

[44] T. Belytschko, H. Stolarski, W. Liu, N. Carpenter, J.-J. Ong, Stress projection for membrane and shear locking in shell finite elements, Computer Methods in Applied Mechanics and Engineering 51 (1985) 221–258.